Gas Geochemistry at Grande Comore and Mayotte Volcanic Islands (Comoros Archipelago), Indian Ocean

Marco Liuzzo, Andrea Di Muro, Andrea Luca Rizzo, Antonio Caracausi, Fausto Grassa, Nicolas Fournier, Bafakih Shafik, Guillaume Boudoire, Massimo Coltorti, Manuel Moreira, et al.

Geochemistry, Geophysics, Geosystems

RESEARCH ARTICLE
10.1029/2021GC009870

Gas Geochemistry at Grande Comore and Mayotte Volcanic Islands (Comoros Archipelago), Indian Ocean

Marco Liuzzo[1,6], Andrea Di Muro[7,2], Andrea Luca Rizzo[1], Antonio Caracausi[1], Fausto Grassa[1], Nicolas Fournier[3], Bafakih Shafik[4], Guillaume Boudoire[1,5], Massimo Coltorti[6], Manuel Moreira[8], and Francesco Italiano[1]

[1]Istituto Nazionale di Geofisica e Vulcanologia, Sezione di Palermo, Palermo, Italy, [2]Institut de Physique du Globe de Paris, CNRS, Université de Paris, Paris, France, [3]Observatoire Volcanologique du Piton de la Fournaise, Institut de Physique du Globe de Paris, La Plaine des Cafres, France, [4]GNS Science, Taupo, New Zealand, [5]Observatoire Volcanologique du Karthala - CNDRS, Moroni, Comoros, [6]Laboratoire Magmas et Volcans, CNRS, IRD, OPGC, Université Clermont Auvergne, Clermont-Ferrand, France, [7]Dipartimento di Fisica e Scienze della Terra, Università di Ferrara, Ferrara, Italy, [8]ISTO, Institut de Sciences de la Terre d' Orléans, Orléans, France

Key Points:

- Map of the spatial distribution of ground CO_2 emissions and its isotopic characteristics in both islands Grande Comore and Mayotte
- Geochemical characterization of fumarolic and hydrothermal gases in terms of both primary component species and isotopic characteristics
- Correlation between the variability of geochemical tracers and the new submarine volcano off Mayotte and its implications for the risk to the island's inhabitants

Supporting Information:

Supporting Information may be found in the online version of this article.

Correspondence to:

M. Liuzzo,
marco.liuzzo@ingv.it

Citation:

Liuzzo, M., Di Muro, A., Rizzo, A. L., Caracausi, A., Grassa, F., Fournier, N., et al. (2021). Gas geochemistry at Grande Comore and Mayotte volcanic islands (Comoros archipelago), Indian Ocean. *Geochemistry, Geophysics, Geosystems*, *22*, e2021GC009870. https://doi.org/10.1029/2021GC009870

Received 28 APR 2021
Accepted 23 JUL 2021

Abstract The Comoros archipelago is an active geodynamic region of intra-plate volcanism within which the youngest and oldest islands (Grande Comore and Mayotte respectively) are characterized by recent volcanic activity. The frequent eruptions of the large shield volcano Karthala on Grande Comore (last eruption 2007), and the recent birth of a large submarine volcano since 2018 at the submarine base of Mayotte are associated with permanent fumarolic emissions, bubbling gas seeps, and soil gas emissions, which are studied in detail here for the first time. CO_2 fluxes and chemical and isotopic gas compositions acquired during two surveys in 2017 and 2020 are integrated with older data sets collected between 2005 and 2016, permitting the identification of a possible influence of the recent volcanic and magmatic activity at Mayotte. At Karthala, high gas fluxes with high temperature, and a marked magmatic signature are concentrated close to the summit crater area, while only weaker emissions with a stronger biogenic signature are found on the volcano flanks. At Mayotte, lower temperature and higher CH_4 content are recorded in two main seep areas of CO_2-rich fluid bubbling, while soil emissions on land record a higher proportion of magmatic fluids compared to Karthala. Our preliminary results reveal two quite separate gas emission patterns for each island that are distinct in composition and isotopic signatures, and well correlated with the present state of volcanic activity. This work may potentially provide support for local observation infrastructures and contribute to the improvement in volcanic and environmental monitoring.

1. Introduction

Comoros archipelago is located in the Mozambique Channel between the east coast of Africa and the north-western coast of Madagascar. The formation of a huge submarine volcanic edifice since 2018, about 50 km offshore east of Mayotte, has prompted a renewal of multidisciplinary researches on the seismo-volcanic activity of the Comoros archipelago by the international volcanological community (Bachèlery et al., 2019; Berthod et al., 2020; Cesca et al., 2020; Feuillet et al., 2019; Lemoine et al., 2020; REVOSIMA, 2019). The archipelago consists of four main islands from NW to SE: Grande Comore, Mohéli, Anjouan, and Mayotte (Figure 1), amongst which Grande Comore hosts the large and frequently active basaltic Karthala volcano (last eruption in 2007). Subaerial Holocene volcanic activity related to a range of alkaline magma compositions (from basanite to phonolite) has been documented in the other islands (Bachèlery et al., 2016; Michon, 2016; Tzevahirtzian et al., 2021 and references therein). Comoros archipelago is considered as the potential diffuse Lwandle-Somali sub-plate boundary and part of the SE extension of the East African Rift System (Famin et al., 2020; Michon, 2016). The recent review of morphological, geological and chronological data of Tzevahirtzian et al. (2021) suggests that Mayotte and Moheli are the oldest islands, while Anjouan and Grande Comore are the most recent ones. The recent volcanism of Karthala in Grande Comore has been interpreted as hot spot related by geochemical studies (e.g., Class et al., 1998). Grande Comore and Anjouan are high altitude volcanic islands, intersected by well developed triple-armed volcanic rifts. On the contrary, Moheli and Mayotte are lower islands, with less well developed rift zones, and a wide insular shelf, which is very narrow on Grande Comore and Anjouan. Karthala is the second most active volcano in the Indian Ocean, after Piton de la Fournaise in La Réunion island, with permanent hydrothermal

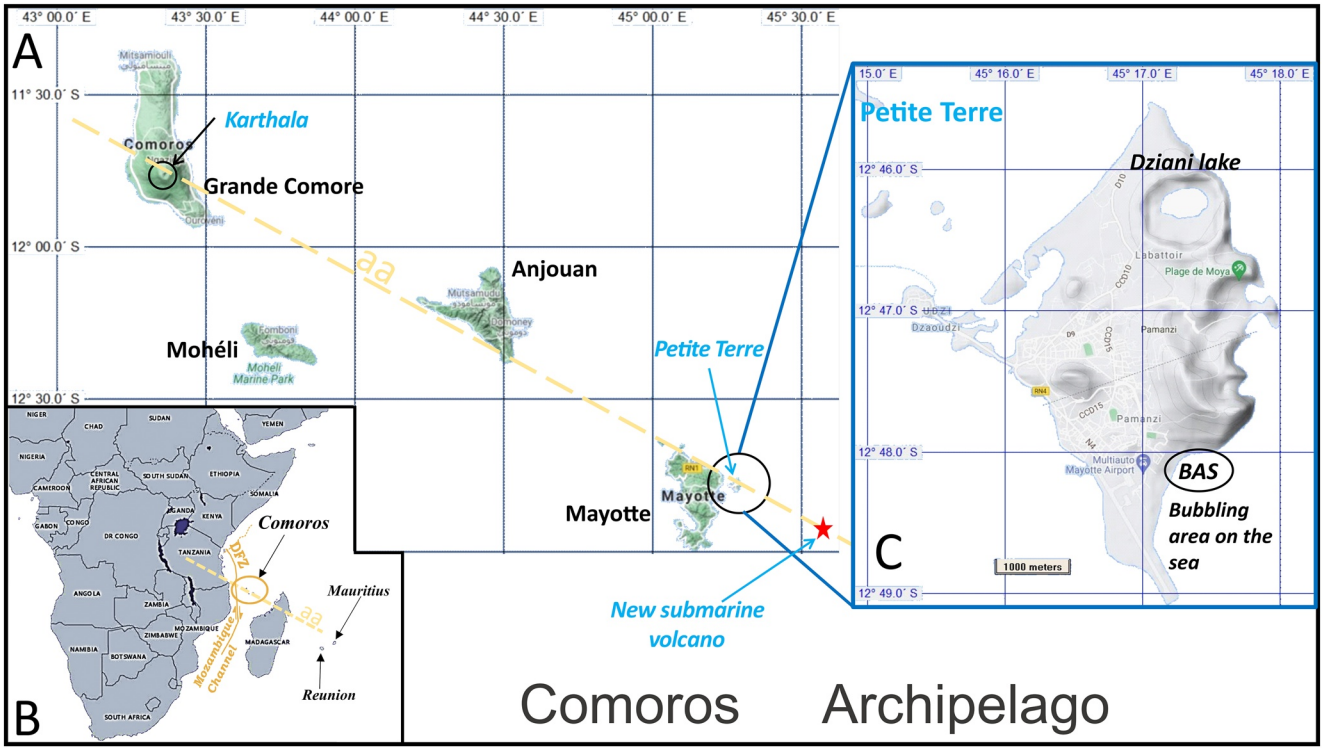

Figure 1. Map of the Comoros archipelago, which is located on the northern zone of the Mozambique Channel (a), in which is also shown the Davie Fracture zone (DZF). The elongated trend N120° "a-a" of the islands (b) corresponds to the recognized regional structural trend well defined by distribution of the 1901–2018 seismicity for $M > 4$ in Lemoine et al. (2020). In (c) highlighted on the map is the little island on the east coast of Mayotte called Petite Terre, where have been acquired all the measurements (both from the soil and from the bubbling area on the sea) mentioned in this paper regarding Mayotte island. The red star is the approximate location of the new submarine volcano.

and fumarolic emissions close to its summit area (Bachèlery & Coudray, 1993; Bernabeu et al., 2018). Two years after the last summit Karthala eruption, Bernabeu et al. (2018) document high CO_2 fluxes in the soil close to the eruptive vent. However, the absence of chemical or isotopic analysis did not permit to attribute these emissions to the recently emplaced magma or to deeper sources. Seep areas of low-temperature CO_2-rich bubbling gases have been reported for the first time between 1993 and 1998 at Mayotte, on the small island (Petite Terre) located on its eastern side (Traineau et al., 2006 and references therein).

In this work, we focus on the gaseous emissions on the oldest (Mayotte) and youngest (Grande Comore) islands, which are also the two recently active volcanic systems of the Comoros archipelago, with the aim at constraining the extent and spatial distribution of the outgassing areas and the geochemical signature of the gas emissions. Data were collected by a team of researchers from IPGP/OVPF and INGV who carried out surveys on the two islands between 2017 and 2020. In addition, we included data from older measurement campaigns which were undertaken for different purposes between 2005 and 2014. The results of the geochemical investigation highlight the differences in outgassing characteristics between the two volcanic islands and their link with the recent volcanic activity. We perform a comparison with the gas geochemistry of La Réunion island, where a deep and plume-like undegassed mantle contribution has long been identified.

Grande Comore and Mayotte are densely populated islands and in view of the high level of seismic and volcanic activity and the related hazards, these first results represent a significant contribution to pave the way for future activities on geochemical monitoring and hazard mitigation.

2. Geological Context

The islands of the Comorian archipelago are located within the Mozambique Channel in a particularly complex geodynamic region where the tectonic features are yet to be unambiguously defined. The main and better known tectonic structure, the Davie Fracture Zone (DFZ) (Phethean et al., 2016), is considered the kinematic hinge that allowed the southward drift of Madagascar following the Gondwana breakup. Despite its well defined structure, the DFZ has been described as either a western transform fault (Coffin et al., 1986) or as a continent-ocean transform margin (Gaina et al., 2013) of the Western Somali Basin (Figure 1a). The alignment of the islands is NW-SE (Figure 1b) and coincident with the main seismic zone of the archipelago (Lemoine et al., 2020). This orientation of islands separates the North Somali basin, which is agreed to be oceanic, and the South Somali basin, which for some authors is thought to be oceanic crust (e.g., Klimke et al., 2016; Rabinowitz et al., 1983), while other authors identify this as a thinned continental crust (e.g., Bassias & Leclaire, 1990; Roach et al., 2017).

The two main hypotheses that have been developed over time to explain the origin of the Comoros volcanism are:

1. a mantle plume, which interacts with the oceanic lithosphere (Class et al., 2005; Claude-Ivanaj et al., 1998; Deniel, 1998; Emerick & Duncan, 1982; Hajash & Armstrong, 1972; Nougier et al., 1986). The link with a deep mantle hot spot has been invoked to explain the eastward migration of volcanism age, but also to explain the variability of geochemical magma composition measured along the archipelago. Karthala lavas are those recording a stronger hot spot signature (Bachèlery & Hémond, 2016; Class et al., 2009; Claude-Ivanaj et al., 1998; Coltorti et al., 1999). Recent seismic tomography (French & Romanowicz, 2015) fails to unambiguously identify a deep plume rooted in the mantle below Comoros archipelago.
2. the reactivation of regional lithospheric structures, which interact with asthenospheric processes. This hypothesis rejects the previous model because it is inconsistent with the current volcanic activity which includes both Karthala volcano and the recent and still ongoing submarine volcanic activity eastward of Mayotte and with the absence of a clear age decrease along the archipelago (Famin et al., 2020; Lemoine et al., 2020; Michon, 2016; Nougier et al., 1986; Tzevahirtzian et al., 2021).

At Mayotte, the volcanic activity becomes increasingly older from the eastern side (Petite Terre island), to the western main island (Grande Terre) (Nehlig et al., 2013). The still ongoing (at the time of writing), large-volume and long-lasting sub-marine eruption of Mayotte, the largest submarine event ever detected by monitoring networks (Cesca et al., 2020; Lemoine et al., 2020), challenges current models on the origin of Comoros volcanism. Since 2018, several km^3 of evolved basanite lava have been emitted on the 3.5 km deep seafloor 50 km east from Mayotte from a deep source located in the upper lithospheric mantle (Bachèlery et al., 2019; Berthod et al., 2020; Lemoine et al., 2020). The new volcano grows on a N120° oriented volcanic ridge, which runs along the eastern submarine flank of Mayotte and whose western subaerial tip is the small island of Petite Terre (Tzevahirtzian et al., 2021; Figure 1b). On Petite Terre, recent volcanic activity has built on the coral reef a set of Holocene basaltic scoria cones and phonolitic maars (Nehlig et al., 2013; Zinke et al., 2001), and two main areas of low-temperature CO_2-rich gas bubbling seeps. A first bubbling area occurs in the NE part of Petite Terre inside the intracrateric lake of the Dziani phonolitic maar, where several CO_2- and CH_4- rich bubbling spots have been identified (Milesi et al., 2020). A second area, first described in 1998 on the eastern tidal flat of Petite Terre is located close to the "Airport beach" (BAS site; Sanjuan et al., 2008; Traineau et al., 2006). There, tens of bubbling spots occur at the southern feet of the large "Vigie" phonolitic maar, on a muddy flat area exposed to significant tide and extended for about 250 × 300 m from the beach (see also Figure 6b).

In Grande Comore, at least three volcanic massifs have been identified: the old and inactive M'Badjini massif in the southernmost part of Grande Comore, the rarely active La Grille volcano in the north (last dated eruption: 1029–1424 CE) and in between the frequently active Karthala shield volcano (last eruption: 2007) (Bachèlery et al., 2016 and references therein). Karthala volcano is a large (summit elevation 2,361 m) basaltic shield volcano, the highest relief of the Comoros archipelago, and exhibits well-developed rift zones diverging from a 3.6 × 2.7 km wide summit polylobate caldera. The average frequency of its eruptions, occurring both at the volcano summit and on the flanks, is of one eruption every 6–8 years over the past 100 years

and the volcano was frequently active in the 1991–2007 period (Bachèlery et al., 2016). The self-potential studies of the summit caldera performed by Lénat et al. (1998) and Bernabeu et al. (2018) show that the main hydrothermal activity of the volcano does not occur below the main summit crater (Choungou-Chahalé), but on the northern part of the summit caldera, where several recent eruptions have occurred. We sampled two main areas, the first one corresponds to steaming grounds and fumaroles located close to the Choungou-Chagnoumeni pit crater located in the northern part of the caldera and filled by the lavas of the last eruption in 2007 (see Figure 5b site CC) and a second one, the "Soufriére" fumarolic area located on recent lavas 1.7 km north of the summit caldera, along the northern rift zone (see Figure 5b site LS).

3. Materials and Methods

3.1. Previous Data Sets

In this study, we present the results of our 2017–2020 surveys on soil gas fluxes and their composition as well as on the composition of Mayotte gas bubbling and Grande Comore fumarolic areas (Figures 5 and 6). Our data set is integrated with older and partly unpublished surveys acquired on the two islands.

At Mayotte, the BAS bubbling site has been first studied by BRGM in November 2005 (Traineau et al., 2006; BRGM report) and April 2008 (Sanjuan et al., 2008; BRGM report) in terms of spatial distribution, gas fluxes, temperature, pH and chemical and isotopic composition. In the BRGM campaigns, $\delta^{13}C$ and δD data were not acquired on methane and preliminary noble gases data were produced by the IPGP laboratory (M. Moreira). A rich biological, chemical and isotopic data set (C-H-S species, not including the noble gases) of the Dziani intracrateric lake and of its bubbling was acquired in the period 2012–2018 (Cadeau et al., 2020; Gérard et al., 2018; Hugoni et al., 2018; Jovovic et al., 2017; Leboulanger et al., 2017; Milesi et al., 2019, 2020). Milesi et al. (2020) collected fluids in August 2016 by focusing on the spatial distribution and C-H chemical and isotopic composition of bubbling gases in the Dziani lake, while only a single analysis (G7 sample) is reported for the BAS area.

On Karthala volcano, the summit steaming grounds and fumarole have been first described (but not sampled) by Bachèlery and Coudray (1993). Soil CO_2 and temperature profiles were measured between March 2008 and January 2010 in the hot grounds (40–80°C) close to the summit 2007 pit crater by Bernabeu et al. (2018). The first detailed study of the gas emissions in Grande Comore was performed in 2014 in the frame of an international geothermal exploration project (Benavente & Brotheridge; Chaheire et al., 2016).

3.2. Gas Sampling and Analysis

Grande Comore field work were performed in December 2017 (volcano flanks) and October 2018 (volcano flanks and summit area). Mayotte surveys were carried out on Petite Terre (Figure 1) in four campaigns, that is, in December 2018, April 2019, September 2019, and November 2020 (Tables 1 and 2).

Soil gas samples for isotopic ($\delta^{13}C$ in CO_2) and chemistry analysis were collected by introducing a steel probe into the ground (50 cm long) and collected in 10 mL Exetainer glass vials and in two-stopcock glass bottles 100 mL.

Dry gases from fumarolic fields at Karthala were collected using a steel probe (the same as for soil sampling) introduced into the ground and connected to a three-way valve equipped of a syringe and a tube connected to the bottles for gas storage. Bubbling gases at Mayotte have been taken using a steel funnel connected to a three-way valve equipped with a syringe and a tube connected to two-stopcock glass bottles 250 mL (chemistry and C-H isotopic analysis), two-stopcock steel bottles 100 mL (noble gases elemental and isotopic analysis), and pre-weighed evacuated bottles containing absorbing alkaline solution (4N NaOH) following the method of Giggenbach and Goguel (1989).

All the gas samples were analyzed at the laboratories of INGV (Istituto Nazionale di Geofisica e Vulcanologia), Sezione di Palermo, for their chemistry and for the isotopic compositions of noble gases (He, Ne, and Ar), C of CO_2, and C and H of CH_4. Analyses are reported in Table 1. The chemical composition of He, H_2, O_2, N_2, CO, CH_4, and CO_2 was measured by a gas chromatograph (Clarus 500, Perkin Elmer) equipped

Table 1
Chemical Composition of Major and Minor Gaseous Components and Isotopic Values From Fumaroles, Bubbling Area and Soil Emission of Grande Comore and Mayotte

					Major (raw)								$\delta^{13}C$ (‰)		δD (‰)
Sampling date	Sample	Lat	Long	Site	T (°C)	CO_2 (vol%)	CO (ppmv)	CH_4 (ppmv)	N_2 (vol%)	O_2 (vol %)	H_2 (ppmv)	He (ppmv)	CO_2	CH_4	CH_4
08/09/2019	Dist N	−12.80064	45.28883	BAS		97.1		2854.0	0.3	0.04		25.0	−4.1	−21.6	
08/09/2019	Dist N	−12.80064	45.28883	BAS		98.5		2982.0	0.4	0.04	112.0	26.0	−4.0	−21.8	
08/09/2019	C1-2	−12.80015	45.28736	BAS		98.7		2444.0	0.3	0.06		29.0	−4.7	−21.0	
08/09/2019	C1-2	−12.80015	45.28736	BAS		97.3		2384.0	0.5	0.07	16.0	28.0	−4.7	−19.2	
13/09/2019	Dist 2	−12.8005	45.28871	BAS		98.3	1.2	2914.0	0.3	0.10		27.0	−3.8	−22.0	
08/09/2019	DIST-1	−12.80064	45.28883	BAS			18.0	390000.0	43.1	15.81	8.0	3558.0		−22.1	−137.8
08/09/2019	C1-2	−12.80015	45.28736	BAS			4.1	455400.0	48.0	2.96	11.0	5528.0		−19.6	−118.1
06/04/2019	Dist 1-A	−12.80064	45.28883	BAS	39.2	97.1	1.2	2442.0	0.5	0.16	<1	21.0	−3.7	−24.4	
06/04/2019	Dist 1-B	−12.80064	45.28883	BAS	39.1	95.8	2.4	2426.0	1.7	0.51	<1	20.0	−3.6		
06/04/2019	Dist 2	−12.8005	45.28871	BAS	nd	97.3	2.1	2406.0	0.3	0.11	<1	19.0	−3.5	−21.4	
06/04/2019	C 1 -1	−12.80015	45.28736	BAS	43	97.0	2.1	2088.0	0.8	0.20	<1	23.0	−4.2	−19.0	
06/04/2019	C 1 -3	−12.80015	45.28736	BAS	43.2	97.0	5.0	2036.0	0.9	0.21	<1	23.0	−4.3	−19.0	
06/04/2019	MAR 3	−12.80051	45.28740	BAS	42	96.5	10.0	2725.0	1.6	0.36	<1	27.0	−4.2	−21.0	
16/12/2018	MAR-1	−12.80036	45.28766	BAS	30.2	63.3	1.6	1209.0	27.8	7.50	2.2	7.0			
16/12/2018	MAR-1	−12.80036	45.28766	BAS	30.2								−4.8		
16/12/2018	CI-1a	−12.80015	45.28736	BAS	29.5	28.7	2.1	416.0	55.0	14.95	<1	bdl	−4.5	−18.7	
16/12/2018	C1-b	−12.80015	45.28736	BAS	29.5	97.9	1.7	2130.0	0.7	0.10	318.0	23.0	−4.5		
16/12/2018	CI-1	−12.80015	45.28736	BAS	29.5								−4.9		
16/12/2018	CI-2	−12.80015	45.28736	BAS	29.4										
16/12/2018	MAN-1	−12.80064	45.28705	BAS	30.1	95.5	0.7	4587.0	2.5	0.21	<1	107.0	−5.1	−12.4	
16/12/2018	MAN-1	−12.80064	45.28705	BAS	30.1								−5.6		
16/12/2018	MAN-2	−12.80064	45.28705	BAS	30.1	83.5	8.0	4621.0	12.0	2.69	<1	110.0	−5.0	−11.7	
16/12/2018	MAN-2	−12.80064	45.28705	BAS	30.1								−5.7		
12/10/2018	Karthala 1	−11.75833	43.360518	CC		50.3	74.9	40.7	37.1	9.38	63.2	16.6	−4.9		
12/10/2018	Karthala 2	−11.75834	43.360379	CC		39.9	23.1	0.0	44.9	11.53	88.1	13.5	−4.5		
13/10/2018	Ka-Su-01	−11.73217	43.363274	LS		92.2	24.1	345.8	1.0	0.21	25992.2	12.7	−4.6		
13/10/2018	Ka-Su-02	−11.73222	43.363317	LS		53.5	22.6	149.6	33.4	8.71	14000.0	12.3	−3.9		
13/10/2018	Ka-Su-03	−11.73334	43.364004	LS		46.6	15.5	145.8	39.6	10.13	11600.0	9.5	−5.0		

			Noble gases isotopes											
Sampling date	Sample	Site	R/Ra	$^4He/^{20}Ne$	^4He (ppm)	^{20}Ne (ppm)	Rc/Ra	^{40}Ar (ppm)	^{38}Ar (ppm)	^{36}Ar (ppm)	$^{40}Ar^*$ (ppm)	^{40}Ar atm	$^{40}Ar/^{36}Ar$ corr	$^{38}Ar/^{36}Ar$ corr
08/09/2019	Dist N	BAS	6.9	329.4	24.4	0.07	6.9	59.3	0.028	0.15	14.9	44.4	392.0	0.1863
08/09/2019	Dist N	BAS	6.9	261.6	25.1	0.10	6.9	55.2	0.025	0.13	16.4	38.8	418.0	0.1878
08/09/2019	C1-2	BAS	7.2	529.1	27.5	0.05	7.2	62.8	0.027	0.14	20.2	42.6	434.1	0.1872
08/09/2019	C1-2	BAS	7.1	152.4	26.0	0.17	7.1	125.3	0.067	0.36	19.6	105.7	348.1	0.1871
13/09/2019	Dist 2	BAS	7.2	310.7	25.7	0.08	7.2	72.0	0.036	0.19	15.4	56.6	374.4	0.1865
08/09/2019	DIST-1	BAS												
08/09/2019	C1-2	BAS												
06/04/2019	Dist 1-A	BAS	7.1	167.7	21.2	0.13	7.1	87.3	0.045	0.24	15.1	72.2	354.9	0.1856

Table 1
Continued

Sampling date	Sample	Site	Noble gases isotopes											
			R/Ra	$^{4}He/^{20}Ne$	^{4}He (ppm)	^{20}Ne (ppm)	Rc/Ra	^{40}Ar (ppm)	^{38}Ar (ppm)	^{36}Ar (ppm)	$^{40}Ar^{*}$ (ppm)	^{40}Ar atm	$^{40}Ar/^{36}Ar$ corr	$^{38}Ar/^{36}Ar$ corr
06/04/2019	Dist 1-B	BAS		1663.9										
06/04/2019	Dist 2	BAS												
06/04/2019	C 1 -1	BAS	7.5	219.3	22.5	0.10	7.5	105.5	0.055	0.30	16.2	89.3	347.4	0.1842
06/04/2019	C 1 -3	BAS	7.3	138.9	22.5	0.16	7.3	141.9	0.079	0.43	15.9	126.0	331.8	0.1852
06/04/2019	MAR 3	BAS	7.2	107.8	27.2	0.25	7.3	239.0	0.139	0.75	17.4	221.5	318.1	0.1861
16/12/2018	MAR-1	BAS	3.2	1.1	8.2	7.65	4.2	3346.6	2.146	11.53	–	–	290.7	0.1861
16/12/2018	MAR-1	BAS												
16/12/2018	CI-1a	BAS												
16/12/2018	C1-b	BAS	7.1	200.3	23.2	0.12	7.1	75.1	0.035	0.19	18.5	56.6	390.3	0.1875
16/12/2018	CI-1	BAS												
16/12/2018	CI-2	BAS												
16/12/2018	MAN-1	BAS	6.4	222.2	102.0	0.46	6.4	497.8	0.263	1.41	81.3	416.4	352.8	0.1873
16/12/2018	MAN-1	BAS												
16/12/2018	MAN-2	BAS	6.9	43.6	113.3	2.60	7.0	1762.8	1.072	5.71	74.6	1688.2	308.8	0.1879
16/12/2018	MAN-2	BAS												
12/10/2018	Karthala 1	CC	5.0	1.7	12.3	7.11	5.9	3827.3	2.475	13.06			296.3	0.1894
12/10/2018	Karthala 2	CC	4.8	1.5	12.7	8.75	5.8	5152.8	3.301	17.42			295.9	0.1894
13/10/2018	Ka-Su-01	LS	5.7	356.6	11.9	0.03	5.7	32.9	0.013	0.08	8.5		378.3	0.1810
13/10/2018	Ka-Su-02	LS	3.8	1.3	10.4	7.88	4.7	5047.3	3.068	16.38			308.3	0.1872
13/10/2018	Ka-Su-03	LS	4.4	1.4	10.0	7.06	5.4	4450.6	2.671	14.26			312.3	0.1873

Sampling date	Sample	Site	Corrected for air contamination					
			He (ppm)	H_2 (ppm)	N_2 (%)	CH_4 (ppm)	CO (ppm)	CO_2 (%)
08/09/2019	Dist N	BAS	25.6		0.15	2925.3		99.6
08/09/2019	Dist N	BAS	26.2	113.0	0.29	3008.4		99.4
08/09/2019	C1-2	BAS	29.3		0.12	2467.3		99.6
08/09/2019	C1-2	BAS	28.6	16.4	0.22	2438.3		99.5
13/09/2019	Dist 2	BAS	27.4			2958.4	1.22	99.8
08/09/2019	DIST-1	BAS						
08/09/2019	C1-2	BAS						
06/04/2019	Dist 1-A	BAS	21.6			2512.6	1.23	99.9
06/04/2019	Dist 1-B	BAS	20.7			2532.0	2.50	100.0
06/04/2019	Dist 2	BAS	19.5			2469.4	2.15	99.8
06/04/2019	C 1 -1	BAS	23.6		0.01	2148.0	2.16	99.8
06/04/2019	C 1 -3	BAS	23.6		0.14	2090.7	5.13	99.6
06/04/2019	MAR 3	BAS	27.7		0.22	2809.4	10.31	99.5
16/12/2018	MAR-1	BAS						
16/12/2018	MAR-1	BAS						
16/12/2018	CI-1a	BAS						
16/12/2018	C1-b	BAS	23.3	322.8	0.38	2162.0	1.72	99.4
16/12/2018	CI-1	BAS						

Table 1
Continued

Sampling date	Sample	Site	Corrected for air contamination					
			He (ppm)	H_2 (ppm)	N_2 (%)	CH_4 (ppm)	CO (ppm)	CO_2 (%)
16/12/2018	CI-2	BAS						
16/12/2018	MAN-1	BAS	109.6		1.72	4699.5	0.71	97.8
16/12/2018	MAN-1	BAS						
16/12/2018	MAN-2	BAS	127.3		2.27	5378.5	9.27	97.2
16/12/2018	MAN-2	BAS						
12/10/2018	Karthala 1	CC	27.1	120.1	4.00	76.2	142.71	96.0
12/10/2018	Karthala 2	CC						
13/10/2018	Ka-Su-01	LS	13.3	27324.5	0.27	363.5	25.37	97.0
13/10/2018	Ka-Su-02	LS	18.1	25073.9	1.60	266.6	40.24	95.9
13/10/2018	Ka-Su-03	LS	14.0	23402.3	3.71	292.4	31.05	93.9

Sampling date	Sample	Lat	Long	Site	Major (raw)								$\delta^{13}C$ (‰)
					T (°C)	CO_2 (vol%)	CO (ppmv)	CH_4 (ppmv)	N_2 (vol%)	O_2 (vol %)	H_2 (ppmv)	He (ppmv)	CO_2
05/12/2017	KA171206 1A	−11.733	43.241	Soil		1.1	13.0	0.5	78.2	19.57	163.0		−22.3
06/12/2017	KA171205 1A	−11.626	43.309	Soil		1.0	9.0	0.5	78.5	19.18	126.0		−25.0
07/12/2017	KA171207 1B	−11.846	43.306	Soil		3.7	7.0	0.5	78.4	16.79	125.0		−23.5
12/10/2018	KART 181012 -1	−11.757155	43.360631	Soil		3.0	16.6	336.0	80.0	21.40	44.0	10.7	−4.2
15/10/2018	KART 64 A	−11.780161	43.267323	Soil		0.5	5.2	2.8	78.2	20.70	25.3	8.4	−23.2
15/10/2018	KART 61 A	−11.626042	43.30893	Soil		3.5	7.8	2.9	70.1	17.74	24.8	10.5	−21.3
15/10/2018	KART 47 A	−11.614397	43.355913	Soil		0.4	8.0	2.3	73.1	19.36	22.6	8.7	−23.9
15/10/2018	KART 49 A	−11.613266	43.350659	Soil		0.2	6.7	3.0	72.6	17.49	13.4		−20.8
15/10/2018	KART 63 A	−11.626137	43.308888	Soil		0.8	6.7	4.6	74.5	19.22	25.7	9.0	−23.3
16/10/2018	KART 67 A	−11.758396	43.242995	Soil		0.5	8.4	1.5	74.5	19.64	33.9	15.9	−22.6
09/09/2019	MAY 1582	−12.800208	45.286703	Soil		5.1	7.0	2.5	73.9	19.39	2.8	5.0	−3.1
10/09/2019	AEROPORTO	−12.801281	45.276823	Soil		4.0			76.6	17.26			−12.1
10/09/2019	MAY 1590	−12.800167	45.285713	Soil		0.8	5.0	1.3	76.7	19.92			−14.5
10/09/2019	MAY 1603	−12.799336	45.286335	Soil		1.1	4.7	1.3	76.9	20.12			−7.1
10/09/2019	MAY 1599	−12.799945	45.286118	Soil		0.9	4.4	1.2	76.7	19.84			−14.8
10/09/2019	MAY 1631	−12.799228	45.284923	Soil		17.7	7.0	1.6	65.0	16.04	2.4	4.2	−2.1
15/12/2018	V-1	−12.80019	45.28664	Soil	32.2	5.1	11.0	1.8	74.2	19.54	11.0	bdl	−1.3
15/12/2018	V-2	−12.80019	45.28664	Soil	32.5	1.1	14.0	1.8	76.7	20.39	9.0	bdl	−6.7
15/12/2018	V-3	−12.80019	45.28664	Soil	32.0	20.2	13.0	1.8	62.7	16.24	11.0	bdl	−1.0
15/12/2018	V-4	−12.80019	45.28664	Soil	31.9	25.4	12.0	1.9	57.9	14.86	14.0	bdl	−2.0
16/12/2018	PAF-1	−12.80009	45.28598	Soil		2.0	9.0	1.0	77.6	19.12	5.0	bdl	−19.0
16/12/2018	PAF-2	−12.80013	45.28596	Soil		2.0	9.0	0.8	77.1	19.47	8.0	bdl	−13.0

Sampling date	Sample	Lat	Long	Site	Major (raw)					
					CO_2 (vol%)	CH_4 (ppmv)	N_2 (vol%)	O_2 (vol %)	H_2 (ppmv)	He (ppmv)
16/04/2008	G1			BAS – (BRGM [2008])	97.4	1900.0	0.4	0.58	<50	18.0

Table 1
Continued

Sampling date	Sample	Lat	Long	Site	Major (raw) CO_2 (vol%)	CH_4 (ppmv)	N_2 (vol%)	O_2 (vol %)	H_2 (ppmv)	He (ppmv)
17/04/2008	G2			BAS – (BRGM [2008])	73.3	1900.0	21.9	5.88	<50	22.0
17/04/2008	G3			BAS – (BRGM [2008])	96.7	2300.0	0.4	0.47	<50	18.0
18/04/2008	G4			BAS – (BRGM [2008])	98.0	2700.0	0.4	0.45	<50	25.9
18/04/2008	G5			BAS – (BRGM [2008])	80.7	1600.0	16.4	4.77	<50	9.9
18/11/2005	9a	−12.801715	45.289816	BAS – (BRGM [2008])	87.7	11300.0	9.9	2.69	<50	340.0
23/11/2005	9b	−12.801625	45.289724	BAS – (BRGM [2008])	98.4	3700.0	1.2	0.53	<50	130.0
20/11/2005	9c	−12.800144	45.287327	BAS – (BRGM [2008])	97.1	1900.0	0.6	0.15	<50	130.0
18/11/2005				BAS – (BRGM [2008])	0.1	<50	78.1	20.90	<50	<50
19/11/2005				BAS – (BRGM [2008])	0.4	<50	76.8	20.90	<50	<50
13/07/2010	SKM70			LS – (Benavente and Brotheridge [2015])	93.6	370.0	0.3	0.00	41000.0	11.0
13/07/2010	SKM53			LS – (Benavente and Brotheridge [2015])	94.1	430.0	0.3	0.00	42000.0	13.0
13/07/2010	SKM72			LS – (Benavente and Brotheridge [2015])	93.9	430.0	0.6	0.00	40000.0	12.0
14/07/2010	SKM67			LS – (Benavente and Brotheridge [2015])	63.2	110.0	27.0	6.40	23000.0	9.0
02/09/2014	SKM180 (Fum 4)	−11.75810318	43.36108294	CC – (Benavente and Brotheridge [2015])	37.3		48.7	13.30		11.0
02/09/2014	SKM183 (Fum 6)	−11.73236085	43.36335423	LS – (Benavente and Brotheridge [2015])	94.5	410.0	1.9	0.11	25000.0	13.0
02/09/2014	SKM182 (Fum 6)	−11.73236085	43.36335423	LS – (Benavente and Brotheridge [2015])	94.3	440.0	1.9	0.00	25900.0	13.0
03/09/2014	SKM185 (Fum 7)	−11.73390178	43.36406988	LS – (Benavente and Brotheridge [2015])	41.8		44.4	11.60	13800.0	9.0
03/09/2014	SKM66 (Fum 8)	−11.73390178	43.36406988	LS – (Benavente and Brotheridge [2015])	41.7		44.4	11.60	13800.0	9.0
03/09/2014	SKM72 (Fum 8)	−11.73390178	43.36406988	LS – (Benavente and Brotheridge [2015])	44.5		42.6	10.80	12600.0	9.0

Sampling date	Sample	Site	$\delta^{13}C$ (‰) CO_2	Noble gases isotopes R/Ra	$^4He/^{20}Ne$	^4He (ppm)	^{20}Ne (ppm)	Rc/Ra	^{40}Ar (ppm)	He (ppm)	Corrected for air contamination N_2 (%)	CH_4 (ppm)	CO_2 (%)
16/04/2008	G1	BAS – (BRGM [2008])	−3.6	6.7	1083.0	18.0	0.02	6.7	70.0	18.6		1983.1	101.7
17/04/2008	G2	BAS – (BRGM [2008])	−4.2	6.4	29.0	22.0	0.76	6.4	1900.0	27.9		2585.7	99.8
17/04/2008	G3	BAS – (BRGM [2008])	−3.9	6.6	118.0	18.0	0.15	6.6	80.0	18.7		2405.8	101.2
18/04/2008	G4	BAS – (BRGM [2008])	−3.7	6.7	2750.0	25.9	0.01	6.7	90.0	26.6		2784.5	101.1
18/04/2008	G5	BAS – (BRGM [2008])	−3.8	6.3	8.0	9.9	1.24	6.5	1500.0	11.0		2012.8	101.5
18/11/2005	9a	BAS – (BRGM [2008])				340.0			700.0	382.2		12729.1	98.8
23/11/2005	9b	BAS – (BRGM [2008])	−3.2			130.0			300.0	132.6		3776.8	100.4
20/11/2005	9c	BAS – (BRGM [2008])	−4.3			130.0			100.0	133.5	0.04	1951.8	99.7
18/11/2005		BAS – (BRGM [2008])							9000.0				
19/11/2005		BAS – (BRGM [2008])							9000.0				

Table 1
Continued

Sampling date	Sample	Site	$\delta^{13}C$ (‰)	Noble gases isotopes						Corrected for air contamination		
			CO_2	R/Ra	$^4He/^{20}Ne$	^4He (ppm)	^{20}Ne (ppm)	Rc/Ra	^{40}Ar (ppm)	He (ppm)	N_2 (%)	CH_4 (ppm)	CO_2 (%)
13/07/2010	SKM70	LS – (Benavente and Brotheridge [2015])				11.0			1501.0				
13/07/2010	SKM53	LS – (Benavente and Brotheridge [2015])				13.0			75.0				
13/07/2010	SKM72	LS – (Benavente and Brotheridge [2015])				12.0			140.0				
14/07/2010	SKM67	LS – (Benavente and Brotheridge [2015])				9.0			3199.0				
02/09/2014	SKM180 (Fum 4)	CC – (Benavente and Brotheridge [2015])				11.0			5690.0				
02/09/2014	SKM183 (Fum 6)	LS – (Benavente and Brotheridge [2015])				13.0			230.0				
02/09/2014	SKM182 (Fum 6)	LS – (Benavente and Brotheridge [2015])				13.0			220.0				
03/09/2014	SKM185 (Fum 7)	LS – (Benavente and Brotheridge [2015])				9.0			5310.0				
03/09/2014	SKM66 (Fum 8)	LS – (Benavente and Brotheridge [2015])				9.0			5300.0				
03/09/2014	SKM72 (Fum 8)	LS – (Benavente and Brotheridge [2015])				9.0			5000.0				

with a 3.5-m column (Carboxen 1000) and double detector (hot-wire detector and flame ionization detector [FID]), for which the analytical errors were <3%.

The C-isotope composition of CO_2 (expressed as $\delta^{13}C$ ‰) versus V-PDB (Vienna-Pee Dee Belemnite) was determined using a continuous-flow isotope-ratio mass spectrometer (Thermo Delta Plus XP, Finnigan), connected to a gas chromatograph (Trace GC) and interface (Thermo GC/C III, Finnigan). The gas chromatograph and its column (length = 30 m and i.d. = 0.32 mm; Poraplot-Q) were operated at a constant temperature of 50°C using He as the carrier gas. The analytical errors were <0.1‰ The same instrument has been used for C and H isotope determination in CH_4, where a combustion interface (Thermo GC III, Finnigan) was used to produce CO_2 from CH_4 and a gas-chromatograph/thermal-conversion interface provided online high-temperature conversion of CH_4 into H. The SDs for the $\delta^{13}C$ and δD measurements of CH_4 were <0.2‰ and <2.5‰, respectively.

Noble gas (He, Ne, and Ar) isotopes were analyzed at the noble-gas laboratory at INGV-Palermo. ^3He and ^4He were measured into a split flight tube mass spectrometer (GVI-Helix SFT), after purification of the sample from the major gaseous species and separation from the other noble gases. ^{20}Ne was determined by admitting Ne into a multicollector mass spectrometer (Thermo-Helix MC plus), after purification procedure into a stainless steel ultra-high vacuum line distinct from that of He and Ar, as above described for helium. The $^3He/^4He$ ratio is expressed as R/Ra (being Ra the He isotope ratio of air and equal to $1.39 \cdot 10^{-6}$) with an analytical uncertainty (1σ) below 0.3%. Hereafter we discuss the $^3He/^4He$ ratio corrected for atmospheric contamination using the measured $^4He/^{20}Ne$ ratio (e.g., Sano & Wakita, 1985) that is reported in units of Rc/Ra, as follows:

Table 2
Soil CO_2 Flux (g m^{-2} d^{-1}) Surveys at Grande Comore and Mayotte

	Grande Comore November 4–8, 2014		
	Latitude	Longitude	CO_2 flux (g m^{-2} d^{-1})
1	−11.760030	43.358620	0.00
2	−11.760120	43.358940	992.60
3	−11.760440	43.359140	0.00
4	−11.760070	43.359300	0.00
5	−11.760150	43.359830	5378.00
6	−11.760410	43.360290	8.90
7	−11.760550	43.361020	0.00
8	−11.760560	43.361840	0.00
9	−11.760500	43.362970	0.00
10	−11.760040	43.363590	0.00
11	−11.758290	43.362920	30.20
12	−11.758200	43.362060	0.00
13	−11.757630	43.361340	1242.70
14	−11.758260	43.361440	5.70
15	−11.758390	43.360850	24.50
16	−11.758310	43.360750	153.50
17	−11.758460	43.360220	7.90
18	−11.758430	43.359810	0.00
19	−11.758320	43.359130	21.30
20	−11.758320	43.359790	6931.00
21	−11.756940	43.356410	0.00
22	−11.756960	43.357310	0.00
23	−11.756970	43.358240	0.00
24	−11.756920	43.359290	4.00
25	−11.757020	43.360120	1.30
26	−11.756930	43.361020	4.60
27	−11.756870	43.361130	9811.10
28	−11.756960	43.361920	0.00
29	−11.756930	43.362760	0.00
30	−11.753250	43.364720	0.00
31	−11.753290	43.363780	0.00
32	−11.753240	43.362890	0.00
33	−11.753270	43.361690	0.00
34	−11.753660	43.360930	0.00
35	−11.753490	43.359830	0.00
36	−11.749920	43.361890	0.00
37	−11.749930	43.361090	0.00
38	−11.750010	43.360040	0.00
39	−11.749950	43.359240	0.00
40	−11.749550	43.358340	0.00
41	−11.753260	43.355550	0.00

Table 2
Continued

	Grande Comore November 4–8, 2014		
	Latitude	Longitude	CO_2 flux ($g\ m^{-2}\ d^{-1}$)
42	−11.753240	43.359270	0.00
43	−11.753320	43.358290	0.00
44	−11.753340	43.357310	0.00
45	−11.734620	43.356290	0.00
46	−11.731600	43.356970	0.00
47	−11.728210	43.356650	2.50
48	−11.727900	43.357430	2.60
49	−11.728070	43.358410	1.10
50	−11.727990	43.359880	1.50
51	−11.728090	43.360430	1.40
52	−11.728050	43.361270	1.90
53	−11.727940	43.362010	4.70
54	−11.728060	43.363120	9.10
55	−11.728050	43.363840	3.60
56	−11.727720	43.364480	3.80
57	−11.732320	43.363310	21.50
58	−11.732320	43.363260	796.70
59	−11.732820	43.362400	0.00
60	−11.731670	43.362060	10.10
61	−11.731540	43.361200	6.10
62	−11.731630	43.360350	3.30
63	−11.731850	43.359590	7.20
64	−11.731530	43.357740	4.10
65	−11.735020	43.357890	5.30
66	−11.735290	43.358390	8.10
67	−11.735430	43.359460	4.90
68	−11.735390	43.360180	8.00
69	−11.735350	43.361070	3.20
70	−11.735510	43.362140	1.30
71	−11.735580	43.362880	3.00
72	−11.735400	43.361130	0.00
73	−11.734460	43.361040	0.00
74	−11.733640	43.360980	1.30
75	−11.732860	43.360950	1.60
76	−11.731890	43.360570	5.80
77	−11.730180	43.359770	6.30
78	−11.729260	43.359940	1.80
79	−11.728800	43.360780	1.60
80	−11.730240	43.360810	4.80
81	−11.730710	43.361680	4.80
82	−11.731120	43.362160	6.60

Table 2
Continued

	Grande Comore November 4–8, 2014		
	Latitude	Longitude	CO_2 flux ($g\ m^{-2}\ d^{-1}$)
83	−11.733480	43.362250	2.10
84	−11.734470	43.362340	6.70
85	−11.734260	43.363090	3.40
86	−11.733520	43.363050	2.70
87	−11.732700	43.363090	8.50
88	−11.731730	43.363020	2.80
89	−11.731340	43.363770	6.00
90	−11.731630	43.364810	8.20
91	−11.732660	43.364940	6.10
92	−11.733500	43.365130	7.50
93	−11.734420	43.364980	1.30
94	−11.735480	43.365060	2.90
95	−11.735480	43.364010	5.40
96	−11.734120	43.364140	313.40
97	−11.733950	43.364120	8994.00
98	−11.733710	43.364130	553.70
99	−11.733580	43.364050	175.80
100	−11.733390	43.363960	3046.10
101	−11.732920	43.363410	17364.40
102	−11.732400	43.363310	396.10
103	−11.735470	43.365470	4.50
104	−11.735410	43.366680	4.20
105	−11.735290	43.367860	1.60
106	−11.734920	43.368590	2.70
107	−11.734950	43.369160	1.50
108	−11.735100	43.370020	1.30
109	−11.734880	43.371330	4.30
110	−11.734890	43.372370	0.00
111	−11.731630	43.372480	5.30
112	−11.727760	43.371830	2.70
113	−11.728050	43.370230	3.00
114	−11.728340	43.369200	13.50
115	−11.728570	43.368350	1.30
116	−11.728670	43.367390	2.60
117	−11.728860	43.366670	5.70
118	−11.728690	43.365970	4.80
119	−11.728840	43.365040	4.40
120	−11.729510	43.365180	0.00
121	−11.730080	43.365400	9.00
122	−11.731050	43.365570	1.20
123	−11.731370	43.366580	5.50

Table 2
Continued

	Grande Comore November 4–8, 2014		
	Latitude	Longitude	CO_2 flux ($g\ m^{-2}\ d^{-1}$)
124	−11.731860	43.367570	0.50
125	−11.731190	43.368440	4.00
126	−11.731050	43.369530	1.10
127	−11.731810	43.370240	3.00
128	−11.732570	43.370970	2.20
129	−11.738900	43.372030	4.40
130	−11.738920	43.371310	4.20
131	−11.738890	43.370270	1.60
132	−11.738950	43.369280	2.70
133	−11.738940	43.368460	1.50
134	−11.738900	43.367580	1.30
135	−11.738890	43.366800	4.20
136	−11.738880	43.365750	0.00
137	−11.738770	43.365270	2.50
138	−11.738960	43.363820	1.10
139	−11.738840	43.363260	1.50
140	−11.739020	43.361900	1.40
141	−11.738830	43.361170	1.90
142	−11.738850	43.360300	4.60
143	−11.738890	43.359250	8.90
144	−11.738860	43.358360	3.60
145	−11.738570	43.357640	3.70
146	−11.738800	43.356490	21.10
147	−11.742410	43.360250	1.30
148	−11.742630	43.361150	2.20
149	−11.742560	43.362230	2.90
150	−11.742500	43.363040	7.20
151	−11.742550	43.363730	3.30
152	−11.742620	43.364710	6.00
153	−11.742450	43.365780	10.00
154	−11.742530	43.366600	0.00
155	−11.742480	43.367530	7.80

	Grande Comore November 28–December 7, 2017		
	Latitude	Longitude	CO_2 flux ($g\ m^{-2}\ d^{-1}$)
1	−11.579000	43.311000	32.10
2	−11.525000	43.337000	15.10
3	−11.879000	43.407000	22.66
4	−11.872000	43.399000	18.88
5	−11.735000	43.329000	18.88
6	−11.735000	43.329000	47.20
7	−11.734000	43.328000	33.98

Table 2
Continued

	Grande Comore November 28–December 7, 2017		
	Latitude	Longitude	CO_2 flux ($g\ m^{-2}\ d^{-1}$)
8	−11.733000	43.327000	18.88
9	−11.732000	43.326000	52.86
10	−11.731000	43.326000	45.31
11	−11.730000	43.324000	16.99
12	−11.728000	43.323000	22.66
13	−11.723000	43.250000	24.54
14	−11.725000	43.249000	168.07
15	−11.727000	43.250000	239.87
16	−11.730000	43.250000	32.10
17	−11.730000	43.249000	20.77
18	−11.732000	43.250000	30.21
19	−11.734000	43.249000	33.98
20	−11.737000	43.250000	24.54
21	−11.720000	43.249000	13.22
22	−11.849000	43.332000	20.77
23	−11.849000	43.330000	256.89
24	−11.849000	43.328000	41.54
25	−11.849000	43.328000	98.18
26	−11.848000	43.321000	18.88
27	−11.847000	43.316000	49.09
28	−11.846000	43.314000	79.30
29	−11.847000	43.311000	54.75
30	−11.846000	43.306000	179.40
31	−11.844000	43.303000	22.66
32	−11.842000	43.301000	18.88
33	−11.840000	43.299000	18.88
34	−11.837000	43.297000	11.33
35	−11.833000	43.292000	120.84
36	−11.829000	43.288000	145.40
37	−11.784000	43.271000	30.21
38	−11.780000	43.267000	226.64
39	−11.778000	43.265000	160.51
40	−11.775000	43.264000	457.58
41	−11.719000	43.249000	16.99
42	−11.721000	43.245000	22.66
43	−11.723000	43.245000	16.99
44	−11.727000	43.244000	60.42
45	−11.728000	43.243000	22.66
46	−11.728000	43.240000	22.66
47	−11.730000	43.242000	15.10
48	−11.733000	43.241000	226.64

Table 2
Continued

	Grande Comore November 28–December 7, 2017		
	Latitude	Longitude	CO_2 flux ($g\ m^{-2}\ d^{-1}$)
49	−11.735000	43.240000	118.96
50	−11.737000	43.240000	94.41
51	−11.740000	43.240000	43.42
52	−11.742000	43.239000	16.99
53	−11.747000	43.238000	22.66
54	−11.748000	43.235000	50.98
55	−11.752000	43.236000	52.86
56	−11.759000	43.239000	11.33
57	−11.759000	43.244000	37.76
58	−11.560000	43.273000	9.44
59	−11.566000	43.272000	94.41
60	−11.570000	43.271000	13.22
61	−11.577000	43.269000	18.88
62	−11.584000	43.267000	35.87
63	−11.588000	43.266000	103.85
64	−11.592000	43.266000	109.51
65	−11.597000	43.263000	11.33
66	−11.609000	43.263000	13.22
67	−11.629000	43.307000	20.77
68	−11.626000	43.309000	306.06
69	−11.622000	43.312000	20.77
70	−11.618000	43.314000	135.95
71	−11.616000	43.315000	62.31
72	−11.594000	43.378000	147.29
73	−11.591000	43.382000	16.99
74	−11.429000	43.404000	98.18
75	−11.427000	43.399000	39.65
76	−11.438000	43.399000	120.84
77	−11.447000	43.402000	100.07
78	−11.454000	43.402000	22.66
79	−11.610000	43.365000	16.99
80	−11.612000	43.363000	228.53
81	−11.614000	43.357000	24.54
82	−11.613000	43.350000	24.54
83	−11.610000	43.346000	71.75
84	−11.611000	43.341000	13.22
	Grande Comore October 11–16, 2018		
	Latitude	Longitude	CO_2 flux ($g\ m^{-2}\ d^{-1}$)
1	−11.876616	43.480066	7.55
2	−11.878802	43.481346	7.55
3	−11.879880	43.477517	13.22

Table 2
Continued

	Grande Comore October 11–16, 2018		
	Latitude	Longitude	CO_2 flux ($g\ m^{-2}\ d^{-1}$)
4	−11.879253	43.472302	7.55
5	−11.882023	43.469274	13.22
6	−11.885114	43.468817	9.44
7	−11.884848	43.465353	11.33
8	−11.885446	43.457200	7.55
9	−11.886513	43.452216	18.88
10	−11.888558	43.445997	28.32
11	−11.890019	43.442657	33.98
12	−11.890607	43.440029	22.66
13	−11.893221	43.435186	20.77
14	−11.894565	43.430336	28.32
15	−11.756312	43.355270	7.55
16	−11.758078	43.357018	9.44
17	−11.757963	43.357585	7.55
18	−11.757925	43.357977	9.44
19	−11.758013	43.358559	9.44
20	−11.757705	43.358812	7.55
21	−11.757610	43.359170	16.99
22	−11.757605	43.359566	30.21
23	−11.757513	43.359916	22.66
24	−11.757327	43.360275	11.33
25	−11.757155	43.360631	802.29
26	−11.757020	43.360974	951.98
27	−11.756931	43.361213	45.31
28	−11.756826	43.361449	283.36
29	−11.756816	43.361700	32.10
30	−11.756957	43.362062	9.44
31	−11.757067	43.362450	7.55
32	−11.757152	43.362882	7.55
33	−11.732509	43.363215	15.10
34	−11.637843	43.376308	11.33
35	−11.636014	43.375007	22.66
36	−11.634025	43.373187	7.55
37	−11.632313	43.371923	7.55
38	−11.628818	43.372358	9.44
39	−11.628904	43.372267	13.22
40	−11.627732	43.368685	9.44
41	−11.627151	43.365583	7.55
42	−11.622232	43.365063	5.66
43	−11.619964	43.363529	5.66
44	−11.615842	43.359638	47.20

Table 2
Continued

	Grande Comore October 11–16, 2018		
	Latitude	Longitude	CO_2 flux ($g\ m^{-2}\ d^{-1}$)
45	−11.614397	43.355913	7.55
46	−11.613988	43.352644	7.55
47	−11.613266	43.350659	16.99
48	−11.611125	43.349181	30.21
49	−11.609914	43.345950	11.33
50	−11.612037	43.338725	28.32
51	−11.613682	43.333515	9.44
52	−11.614027	43.329282	7.55
53	−11.614261	43.324552	9.44
54	−11.614549	43.322405	20.77
55	−11.614855	43.317845	20.77
56	−11.615610	43.314634	16.99
57	−11.618371	43.313629	28.32
58	−11.621824	43.312271	9.44
59	−11.626042	43.308930	105.74
60	−11.625871	43.309033	56.64
61	−11.626137	43.308888	120.84
62	−11.780161	43.267323	67.97
63	−11.770174	43.261717	11.33
64	−11.759701	43.256409	37.76
65	−11.758396	43.242995	84.96
	Mayotte September 9–13, 2019		
	Latitude	Longitude	CO_2 flux ($g\ m^{-2}\ d^{-1}$)
1	45.286856	−12.799818	50.66
2	45.286886	−12.799780	3.50
3	45.286808	−12.799860	7.62
4	45.286780	−12.799913	4.02
5	45.286777	−12.799973	9.68
6	45.286748	−12.799982	5.70
7	45.286731	−12.800008	5.66
8	45.286717	−12.800075	3.90
9	45.286699	−12.800123	4.26
10	45.286686	−12.800178	3.95
11	45.286703	−12.800208	30.90
12	45.286661	−12.800261	2.92
13	45.286664	−12.800280	4.80
14	45.286682	−12.800339	2.04
15	45.286693	−12.800380	0.52
16	45.286672	−12.800439	1.64
17	45.286711	−12.800493	2.28
18	45.285713	−12.800167	5.28

Table 2
Continued

	Mayotte September 9–13, 2019		
	Latitude	Longitude	CO_2 flux ($g\ m^{-2}\ d^{-1}$)
19	45.285764	−12.800136	4.86
20	45.285806	−12.800110	12.65
21	45.285844	−12.800085	8.40
22	45.285883	−12.800070	17.57
23	45.285907	−12.800087	5.70
24	45.286072	−12.800006	22.82
25	45.286160	−12.800000	9.00
26	45.286118	−12.799945	17.06
27	45.286107	−12.799880	7.76
28	45.286142	−12.799805	5.36
29	45.286244	−12.799578	21.54
30	45.286335	−12.799336	41.57
31	45.286491	−12.799352	14.70
32	45.286694	−12.799469	19.13
33	45.286883	−12.799525	6.48
34	45.287022	−12.799293	11.90
35	45.287079	−12.799116	8.10
36	45.287149	−12.798782	12.95
37	45.282678	−12.805537	0.45
38	45.282875	−12.805612	1.18
39	45.283069	−12.805955	0.00
40	45.282586	−12.805040	1.63
41	45.282379	−12.805167	1.00
42	45.277490	−12.802276	0.00
43	45.277386	−12.802210	0.00
44	45.277352	−12.802227	0.00
45	45.277246	−12.802167	4.45
46	45.277162	−12.802143	4.36
47	45.277292	−12.802176	1.21
48	45.277152	−12.802055	8.00
49	45.277126	−12.801957	1.64
50	45.277061	−12.801850	0.52
51	45.276823	−12.801281	15.70
52	45.276858	−12.801248	4.21
53	45.284543	−12.799820	11.56
54	45.284848	−12.799386	37.94
55	45.284923	−12.799228	173.44
56	45.285052	−12.799154	39.81
57	45.285033	−12.797719	0.00
58	45.285041	−12.797734	11.98
59	45.284897	−12.797933	4.84

Table 2
Continued

	Mayotte September 9–13, 2019		
	Latitude	Longitude	CO_2 flux ($g\ m^{-2}\ d^{-1}$)
60	45.284909	−12.798320	27.11
61	45.284959	−12.798641	13.28
62	45.284912	−12.798811	42.42
63	45.284776	−12.799008	9.62
64	45.285290	−12.797520	1.69
65	45.285442	−12.797118	2.12
66	45.285659	−12.796799	6.87
67	45.284645	−12.801006	2.36
68	45.284708	−12.800662	3.18
69	45.286793	−12.800945	3.26
70	45.288012	−12.799281	2.55
71	45.287850	−12.799243	0.49
72	45.287528	−12.799367	0.00
73	45.287306	−12.799543	4.04
74	45.287123	−12.799624	1.61
75	45.281475	−12.795606	1.99
76	45.281311	−12.796021	4.06
77	45.281218	−12.796457	6.18
78	45.281190	−12.797037	6.81
79	45.281312	−12.797480	2.53
80	45.281154	−12.798122	2.03
81	45.280780	−12.798222	7.22
82	45.281349	−12.797331	2.60
83	45.282582	−12.798498	5.60
84	45.282209	−12.799108	1.80
85	45.280079	−12.792672	1.06
86	45.279778	−12.793405	1.45
87	45.279577	−12.794203	3.39
88	45.279207	−12.795135	13.83
89	45.279342	−12.795964	0.00
90	45.278689	−12.796682	3.46
91	45.278386	−12.797120	2.67
92	45.278279	−12.797905	16.76
93	45.277967	−12.798124	0.00
94	45.277448	−12.798648	7.81
95	45.255220	−12.782986	1.97
96	45.255288	−12.781948	3.81
97	45.254958	−12.781035	0.00
98	45.257887	−12.783449	2.11
99	45.260400	−12.785424	3.47
100	45.261339	−12.786133	2.61

Table 2
Continued

	Mayotte September 9–13, 2019		
	Latitude	Longitude	CO_2 flux ($g\ m^{-2}\ d^{-1}$)
101	45.262178	−12.786088	0.00
102	45.261778	−12.785416	3.32
103	45.264903	−12.787605	5.05
104	45.268356	−12.789905	5.71
105	45.268894	−12.791590	2.73
106	45.273430	−12.794984	8.00
107	45.274379	−12.794448	5.34
108	45.275029	−12.794076	1.03
109	45.275483	−12.793842	2.43
110	45.275939	−12.793916	7.21
111	45.276297	−12.793910	12.45
112	45.276781	−12.793827	3.11
113	45.277189	−12.793428	2.68
114	45.277539	−12.792994	1.97
115	45.278188	−12.792446	5.57
116	45.280727	−12.766360	0.00
117	45.280762	−12.768051	0.39
118	45.279645	−12.770106	2.52
119	45.279858	−12.771997	3.38
120	45.280814	−12.774220	2.93
121	45.281827	−12.776119	1.50
122	45.294567	−12.783769	1.70
123	45.293457	−12.784258	6.53
124	45.292021	−12.784650	3.35
125	45.290841	−12.785500	26.03
126	45.289486	−12.785186	6.06
127	45.288814	−12.784143	10.06
128	45.288652	−12.783974	11.54
129	45.289141	−12.783073	6.76
130	45.288129	−12.782416	1.27
131	45.286670	−12.781859	4.26
132	45.285204	−12.782200	0.00
133	45.283348	−12.782728	6.09

	Mayotte BAS September 9–13, 2019		
	Latitude	Longitude	CO_2 flux ($g\ m^{-2}\ d^{-1}$)
1	45.288840	−12.800657	33304.40
2	45.288840	−12.800657	33304.40
3	45.288818	−12.800576	29549.64
4	45.288818	−12.800576	29549.64
5	45.288787	−12.800533	20025.38
6	45.288787	−12.800533	20025.38

Table 2
Continued

	Mayotte BAS September 9–13, 2019		
	Latitude	Longitude	CO_2 flux ($g\ m^{-2}\ d^{-1}$)
7	45.288766	−12.800518	21481.59
8	45.288766	−12.800518	21481.59
9	45.288766	−12.800518	21481.59
10	45.288766	−12.800518	21481.59
11	45.288734	−12.800502	34896.13
12	45.288734	−12.800502	34896.13
13	45.288676	−12.800483	22764.99
14	45.288611	−12.800534	27874.64
15	45.288257	−12.799866	12330.93
16	45.288257	−12.799866	12330.93
17	45.288257	−12.799866	12330.93
18	45.288257	−12.799866	12330.93
19	45.288257	−12.799866	12330.93
20	45.288257	−12.799866	12330.93
21	45.288257	−12.799866	12330.93
22	45.288257	−12.799866	12330.93
23	45.288257	−12.799866	12330.93
24	45.288257	−12.799866	12330.93
25	45.288257	−12.799866	12330.93
26	45.288257	−12.799866	12330.93
27	45.287666	−12.800374	35046.24
28	45.287666	−12.800374	35046.24
29	45.287666	−12.800374	35046.24
30	45.287666	−12.800374	35046.24
31	45.287666	−12.800374	35046.24
32	45.287666	−12.800374	35046.24
33	45.287361	−12.800153	18028.15
34	45.287361	−12.800153	18028.15
35	45.287361	−12.800153	18028.15
36	45.287361	−12.800153	18028.15
37	45.287364	−12.800154	47932.23
38	45.287370	−12.800155	12824.78
39	45.287392	−12.800154	13008.43
40	45.287356	−12.800126	18762.74
41	45.287356	−12.800126	18762.74
42	45.287388	−12.800106	23629.43
43	45.287388	−12.800106	23629.43
44	45.287388	−12.800106	23629.43
45	45.287402	−12.800144	136.21
46	45.288553	−12.800236	35046.24
47	45.289069	−12.800259	70485.66

Table 2
Continued

	Mayotte BAS September 9–13, 2019		
	Latitude	Longitude	CO_2 flux ($g\ m^{-2}\ d^{-1}$)
48	45.289104	−12.800310	17064.31
49	45.289178	−12.800359	26435.94
50	45.289290	−12.800481	8730.58
51	45.289524	−12.800485	5952.67
52	45.289584	−12.800270	15537.98
53	45.289039	−12.800000	14289.19
	Mayotte November 11, 2020		
	Latitude	Longitude	CO_2 flux ($g\ m^{-2}\ d^{-1}$)
1	45.28444	−12.7644	4.81
2	45.28326	−12.7654	6.69
3	45.28096	−12.7656	5.95
4	45.28058	−12.7681	15.93
5	45.27964	−12.7702	34.82
6	45.27978	−12.7718	17.22
7	45.28066	−12.7736	26.00
8	45.28116	−12.7753	17.04
9	45.28222	−12.7771	13.72
10	45.28137	−12.7787	16.14
11	45.28062	−12.7801	15.93
12	45.27904	−12.7812	29.44
13	45.27759	−12.7818	39.00
14	45.27644	−12.7828	8.52
15	45.27516	−12.7842	4.78
16	45.27395	−12.7852	48.00
17	45.27289	−12.7863	8.96
18	45.26905	−12.7873	10.93
19	45.26936	−12.7895	19.95
20	45.26946	−12.7896	3.85
21	45.26819	−12.789	7.94
22	45.2847	−12.7824	62.91
23	45.28392	−12.7826	159.30
24	45.28293	−12.7828	28.73
25	45.28168	−12.783	6.07
26	45.28016	−12.7838	48.72
27	45.27952	−12.7842	14.55
28	45.27929	−12.7856	13.95
29	45.2793	−12.7856	37.36
30	45.27905	−12.7868	4.03
31	45.27994	−12.7891	15.85
32	45.28001	−12.7911	12.56
33	45.28612	−12.7999	29.08

Table 3
Synopsis of Soil CO_2 Results and Relative Method Used and Year of Measurements

	Grande Comore	Grande Comore		Mayotte		Mayotte bubbling sea
CO_2 flux [g m^{-2} day^{-1}]	2014	2017	2018	2019	2020	2019
Min	0.0	9.44	5.66	0.0	3.85	12.2
Max	17364.4	457.58	951.98	173.4	159.3	70485.7
Average	365.6	67.61	51.91	8.2	23.90	21084.0
σ	1886.3	79.41	153.91	17.0	28.39	12045.2
	Accumulation Chamber	*Dynamic Concentration (K = 30)*		*Accumulation Chamber*		*Accumulation Chamber*

$$\frac{R}{R^a} = \frac{\left(\frac{R_m}{R_a}\right)\left(\frac{^4He}{^{20}Ne}\right)_m - \left(\frac{^4He}{^{20}Ne}\right)_a}{\left(\frac{^4He}{^{20}Ne}\right)_m - \left(\frac{^4He}{^{20}Ne}\right)_a} \quad (1)$$

where subscripts m and a refer to measured and atmosphere theoretical values, respectively ($[He/Ne]_a = 0.318$) (Ozima & Podosek, 1983). We highlight that the correction on the $^3He/^4He$ ratio is small or negligible for most of the gas samples ($(^4He/^{20}Ne)_m >> (^4He/^{20}Ne)_a$.

The Ar elemental and isotopic compositions (^{36}Ar, ^{38}Ar, and ^{40}Ar) were quantified in a multicollector mass spectrometer (Helix MC-GVI). The analytical uncertainty (1σ) for single $^{40}Ar/^{36}Ar$ measurements was <0.1%. ^{40}Ar was corrected for air contamination ($^{40}Ar^*$) in samples showing $^{40}Ar/^{36}Ar > 315$ assuming that the ^{36}Ar present derived from atmosphere, as follows:

$$^{40}Ar^* = {}^{40}Ar_{\text{sample}} - {}^{36}Ar_{\text{sample}} \cdot \left(\frac{^{40}Ar}{^{36}Ar}\right)_{\text{air}} \quad (2)$$

Typical blanks for He, Ne, and Ar were $<10^{-15}$, $<10^{-16}$, and $<10^{-14}$ mol, respectively, and are at least two orders of magnitude lower than the sample signals at the relative mass spectrometers. Further details on samples purification and analysis are described by Rizzo et al. (2019) and Boudoire et al. (2020).

3.3. Soil CO_2 Fluxes

The soil CO_2 emissions data presented in this study have been acquired drawing on two different methods: accumulation chamber (Chiodini et al., 1998) and dynamic concentration (Gurrieri & Valenza, 1988). The methods differ owing to the fact that different teams carried out measurement surveys on different islands at different times. However, each single measurement campaign is consistent for the method used (Tables 2 and 3).

3.3.1. Accumulation Chamber Method

Both Benavente and Brotheridge (2015) surveys in Grande Comore and two of our surveys at Mayotte (September 2019 and November 2020) adopted the accumulation chamber method for measurements of soil CO_2 flux emissions using two different portable accumulation chamber each of them equipped with different IR spectrometers. Benavente and Brotheridge's campaign used a West System portable instrument with a LI-COR 820 IR and a 200 mm diameter chamber (West System chamber B), which introduces soil gas through the infrared spectrometer via tubing with an inline $Mg(ClO_4)_2$ filter (avoiding the absorption of moisture which may cause interference in CO_2 concentration). Our campaigns in 2019 and 2020 at Mayotte Island used a West Systems portable accumulation chamber equipped with a Dräger Polytron IR sensor and a chamber with the same geometry as the one used by Benavente and Brotheridge in Grande Comore (West system chamber B). We recorded soil temperature at each measurement location using a handheld Type K thermocouple probe inserted to 10 cm below ground level. In addition, pressure measurements and other

weather parameters were recorded by a hand-held instrument meter (Kestrel 5000 series). Soil CO_2 flux (g m^{-2} d^{-1}) from each site were calculated using the following Equation 1:

$$\phi CO_2 = 44.01 \cdot \frac{86400 \cdot P}{10^6 \cdot R \cdot T_k} \cdot \frac{V}{A} \cdot \frac{\delta_c}{\delta_t} \quad (3)$$

where δ_c/δ_t is the change in the CO_2 concentration with time (ppm s^{-1}), P is the measured pressure in mbar, R is the gas constant (bar L K^{-1} mol^{-1}), T is the measured temperature (K), V is the chamber net volume (0.006186 m^3) and A is chamber inlet net area (0.0314 m^2). The measurement accuracy of the CO_2 flux measurements method is ±12.5% (Evans et al., 2001).

3.3.2. Dynamic Concentration Method

In our Grande Comore surveys, we focused on CO_2 soil emissions on the volcano flanks, where the Benavente and Brotheridge (2015) surveys failed in identifying significant anomalies using the accumulation chamber method. Therefore, we performed most of our measurements using the dynamic concentration method in our 2017 and 2018 field works and compared them with a subset acquired on the same sites using the accumulation chamber technique. This approach permits us to compare the Karthala data set with that acquired on the Piton de la Fournaise volcano (Liuzzo et al., 2015). The dynamic concentration method (Gurrieri & Valenza, 1988) is based on an empirically identified relationship between soil CO_2 flux and CO_2 concentration in a gas mixture obtained by diluting soil gas with air (dynamic concentration), by means of a specific 50 cm probe inserted into the soil. Through a constant flux rate of 0.8 l/m, the gas from the soil is pumped to an IR spectrophotometer which measures CO_2 concentration. The spectrophotometer used was manufactured by Edinburgh Instruments Ltd. (range 0%–10%; accuracy ±2%; digital resolution 0.01%) pressure and temperature corrected and it is the same used in the surveys on Piton de la Fournaise volcano. The CO_2 flux is derived from the CO_2 dynamic concentration value through an empirical relationship (4) verified experimentally in the laboratory for a range of applicable permeability 0.36–123 μm^2 and pumping flux 0.4–4.0 L/min:

$$\phi CO_2 = \left(32 - 5.8 \cdot k^{0.24}\right) C_d + 6.3 \cdot k^{0.6} \cdot C_d^3 \quad (4)$$

where ϕCO_2 is the soil CO_2 flux expressed in kg m^{-2} d^{-1}, k is the numerical values of the gas permeability (μm^2), and C_d is the numerical value of molar fraction of the diluted CO_2 concentration. In this work, ϕCO_2 is converted into g m^{-2} d^{-1}. For more details on the method, see Camarda et al. (2006a, 2006b). In this work we used a k value of 30, which is very close to the k value (35) used at Reunion island in previous studies on Piton de la Fournaise (Boudoire et al., 2017; Liuzzo et al., 2013, 2015). In consideration of the typical range of permeability in volcanic soils, $k = 30$ value is a reasonable value limiting the error into less than 7% of the measurement (see Table S1).

4. Results

4.1. Gas Composition of Fumaroles and Bubbling Gases

4.1.1. Chemistry

Karthala gases (CC, from the summit caldera fumaroles; LS from the Soufrière area. For the locations see Figures 5 and 6) show a general higher degree of air contamination with respect to Mayotte samples (Table 1), with the exception of sample Ka-Su-01 from Soufrière that shows the highest CO_2 concentration (up to 92.2%), a significant content of H_2 (25,992 ppm), low concentrations of CH_4 (346 ppm). With regard to noble gases, He varies in a narrow concentration range (10.0–12.7 ppm), ^{20}Ne is between 0.03 (sample Ka-Su-01) and 7.7 ppm, ^{40}Ar 32.8 (sample Ka-Su-01) and 5,152.8 ppm. In the Mayotte sample set noble gases show a variable concentration, with He ranging between 8.2 and 113.2 ppm, ^{20}Ne between 0.052 and 7.65 ppm, ^{40}Ar in the range 55.1–3346.6 ppm. Among the other samples taken from high flux pools, only the sample CI-1a has a significant air contamination, showing concentrations of N_2 and O_2 of 54.9% and 14.9%, respectively. The BAS bubbling gases from the tidal flat show a CO_2 dominant composition up to 98.69% and a variable concentration in CH_4 ranging between 416 and 2,982 ppm. The concentration of CH_4 increases significantly in the "MAN" samples, taken from low-flux pools located close to littoral mangroves (up to

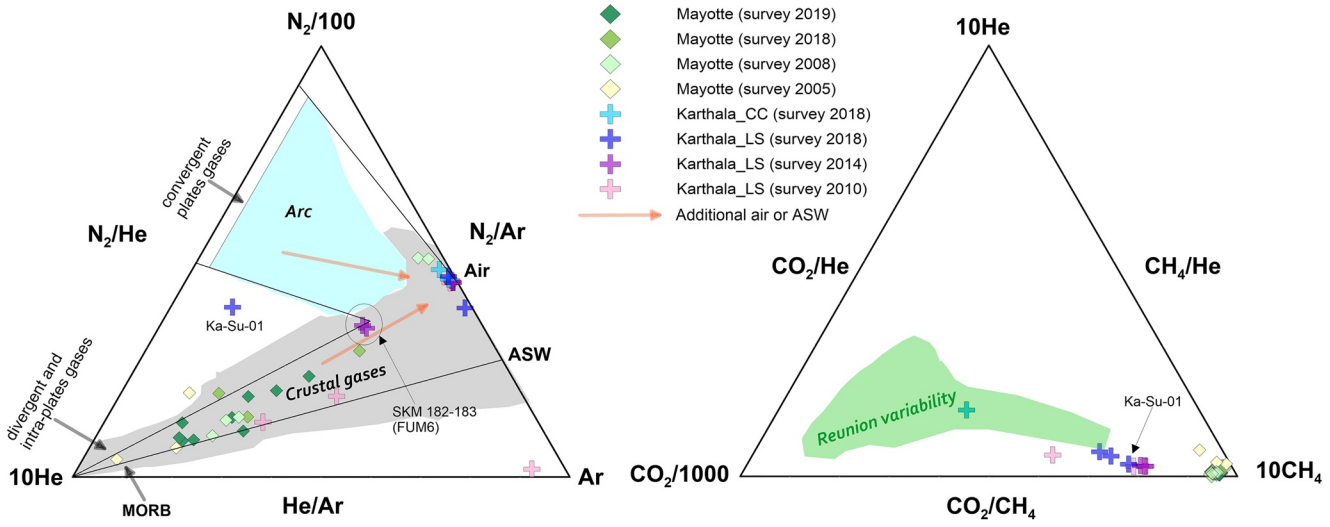

Figure 2. Relative proportion of He-Ar-N_2 in a ternary diagram on the left showing also the areas of crustal gases and arc volcanism from literature. Data collected at Grande Comore and Mayotte show a variable air and ASW contamination. CO_2-CH_4-He ternary diagram on the right displays a relatively CH_4-enrichment of Grande Comore and particularly in Mayotte. For comparison is also shown the field of variability of La Reunion gases.

4,621 ppm). In the BAS samples, H_2 and CO are generally in low concentrations ranging between 2.2 and 318 ppm for H_2 and 0.7 and 18 ppm for CO.

The chemical composition of Karthala and Mayotte gases is plotted in the ternary diagrams of Figure 2. The relative proportions of N_2, He, and Ar, display a mixing trend between a He-rich component and an atmospheric component (air or air-saturated water – ASW). Both gases from the fumarolic Karthala areas (CC and LS) and the bubbling gases from Mayotte (BAS) show a variable degree of contamination by an atmospheric endmember, and its contribution is higher for air than for ASW. On the whole, the He-Ar-N_2 variability falls within a typical compositional range of crustal gases of which the two dominant mixing sources appear to be atmospheric and MORB-type mantle, well distinguished from typical subduction-related gases. An exception is the sample Ka-Su-01 which is significantly different from the present Karthala database, where only the samples SKM182 and SKM183 (fumarole 6 – survey 2014; Benavente & Brotheridge, 2015) show some similarity in low ^{40}Ar and He/N_2 ratio. Another exception is sample SKM70, (sampled in 2010 by Benavente and Brotheridge [2015]), over-enriched in Ar and therefore placed in the corresponding vertex of the ternary diagram. However, the apparent excess in Ar is actually due to an anomalous absence in N_2 (Table 1). This sample can reasonably be considered an outlier in which analytical problems were encountered during lab analysis and therefore will not be discussed further.

The chemical composition in relation to the plot of CO_2-CH_4-He highlights that low temperature gas seeps of Mayotte have a larger CH_4 proportion with respect to Karthala fumarolic gases. In the plot, it is also reported the field of variability of La Reunion bubbling gases that allows to argue that Comoros gases are in general CH_4-enriched.

4.1.2. Isotopic Ratios of Noble Gases, CO_2, and CH_4

Table 1 reports the isotopic compositions of noble gases, CO_2, and CH_4 of the sampled gases. Karthala gases have R/Ra values ranging from 3.8 (Ka-Su-02) to 5.7 Ra (Ka-Su-01), with no significant variation between CC and LS emissions. After correction for the contamination by atmospheric fluids (Rc/Ra), the $^3He/^4He$ value (5.7) is still measured in the sample Ka-Su-01, since it has the minor air contamination. Instead, the other samples range from 4.7 to 5.9 Ra due to a variable atmospheric contribution. In gases from Karthala, the $^4He/^{40}Ar^*$ ratio calculated after the correction of ^{40}Ar for atmospheric contamination (see Equation 2 in Section 3.2) is available only for sample Ka-Su-01 and is 1.5. The relatively higher air contamination in Karthala gases, than in Mayotte gases, is also highlighted by the $^4He/^{20}Ne$ ($^4He/^{20}Ne_{air} = 0.31$), which is generally low with an average of 1.5 (with exception of Ka-Su-01, $^4He/^{20}Ne = 356.6$), and $^{40}Ar/^{36}Ar$ ($^{40}Ar/^{36}Ar_{air} = 295.5$), which is in average 303.2 (with exception of Ka-Su-01, $^{40}Ar/^{36}Ar = 378$).

In the BAS bubbling gases there is the lack of a strong air contamination as previously indicated by the chemistry of these gases since the $^4He/^{20}Ne$ ratios (up to 1,663) are orders of magnitude higher the ratio in air (0.318), therefore no significant changes can be observed in the comparison between R/Ra and Rc/Ra values, except for only one sample (MAR-1) sampled in 2018. In fact, this sample shows a $^3He/^4He$ ratio of 3.2 Ra and a $^3He/^4He$ ratio of 4.2 (Rc/Ra) after correction for air contamination. The latter value strongly differs from the rest of the data set of BAS gases, thus we suspect that this sample underwent some storage and transport to the laboratory issues that fractionated the $^3He/^4He$, leading us to exclude it for the following discussion. In support of this, we highlight that the sample MAR-3 collected in April 2019 from the same degassing area yielded an Rc/Ra value of 7.2 (Table 1). The $^4He/^{40}Ar^*$ values of BAS gases range between 1.2 and 1.7 with a general overlap of the values among the different emissions and surveys. $^4He/^{20}Ne$ in Mayotte samples vary up to 1,660 and only the MAR-1 and MAN-2 ($^4He/^{20}Ne = 1.07$ and 43.59, respectively) samples, both taken from pools with a relatively low flux, show significant air contamination. The variability of $^{40}Ar/^{36}Ar$ span up to 434, with MAR-1 and MAN-2 again showing the highest air contamination ($^{40}Ar/^{36}Ar = 290$ and 308, respectively).

The C-isotope composition of CO_2 ($\delta^{13}C_{CO_2}$) of Karthala gases varies between −4.98‰ and −4.48‰, except for sample Ka-Su-02 that shows the most positive value of −3.91‰. At Mayotte the $\delta^{13}C_{CO_2}$ values of BAS gases vary from −5.74‰ to −3.5‰, whereas the most negative ratios are measured in samples from MAN.

The C and H pair isotope in methane were measured only in BAS gases. In detail, the C-isotope composition of CH_4 ($\delta^{13}C_{CH_4}$) was determined in most of the samples and varies between −24.4‰ and −18.7‰, except for two samples from MAN 1 and 2 that showed the less negative ratios of −12.4‰ and −11.7‰. The hydrogen isotopic composition of CH_4 (δD_{CH4}) was measured only in C1-2 and DIST-1 that were sampled in 2019 through Giggenbach bottles to enrich the concentration of CH_4 of dry gases. These samples yielded a δD of −118.1‰ and–137.8‰ V-SMOW, respectively.

5. Discussion

5.1. Light Noble Gas Signature

Our new He-isotopic data for Karthala and Mayotte span a significant range of $^3He/^4He$ signatures (4.18–7.53 Ra), with systematic differences between the two islands of Comoros archipelago. In detail, gases from Mayotte show Rc/Ra values higher than those from Karthala. Interestingly, the Rc/Ra variability we measured in 2017–2020 gases from Mayotte (7.5–6.4 Ra) and Karthala (5.9–4.7 Ra) matches that found in fluid inclusions from the two active volcanic edifices of the Grande Comore, La Grille, and the Karthala (6.9 and 5.2 Ra respectively; Class et al., 2005). In Figure 3, we modeled two air-magma mixing curves considering data from Class et al. (2005) at Grande Comore and considering the average of the values for La Grille and Karthala fluid inclusions as representative of possible mantle reservoirs end-members. According to Class et al. (1998, 2005, 2009) that propose the presence of a plume contribution in the mantle beneath Gran Comore, our data show that Comoros gases have a low-He signature, like the fluid inclusions in lavas from the same volcanic systems (Karthala volcano). This low $^3He/^4He$ signature is well distinct from that documented in typical hot-spot contexts like the adjacent Afar region (R/Ra up to 19.6; Hilton et al., 2011; Marty et al., 1996) and la Réunion (R/Ra = 14.5–12; Boudoire et al., 2020; Marty et al., 1993). In Figure 3, data of bubbling gases of Piton des Neiges from La Reunion are plotted together with two mixing curves that explain their variability, showing that they fall within the range of Rc/Ra values measured in fluid inclusions of eruptive products of the island.

Ocean island basalts (OIB) from the Comoros archipelago display geochemical features different from the other Indian OIB (Bachèlery & Hemond, 2016; Class & Goldstein, 1997; Class et al., 1998, 2009; Claude-Ivanaj et al., 1998; Deniel, 1998; Pelleter et al., 2014; Späth et al., 1996). Comoros volcanisms has produced a suite of variably silica-undersaturated, alkaline lavas (from melilitites and basanites, to alkali basalts to phonolites), enriched in incompatible trace elements and with variable relative depletion in K. With the exception of La Grille lavas, most lavas on the archipelago record the signature of variable degrees of fractionation during their storage and ascent to the surface after their emission from the deep garnet-bearing mantle source (Bachèlery et al., 2016). Several geochemical models have been proposed to explain the elongated array of their Sr-Nd-Pb isotopic signature, whose end-members range from (a) mixing between heterogeneous

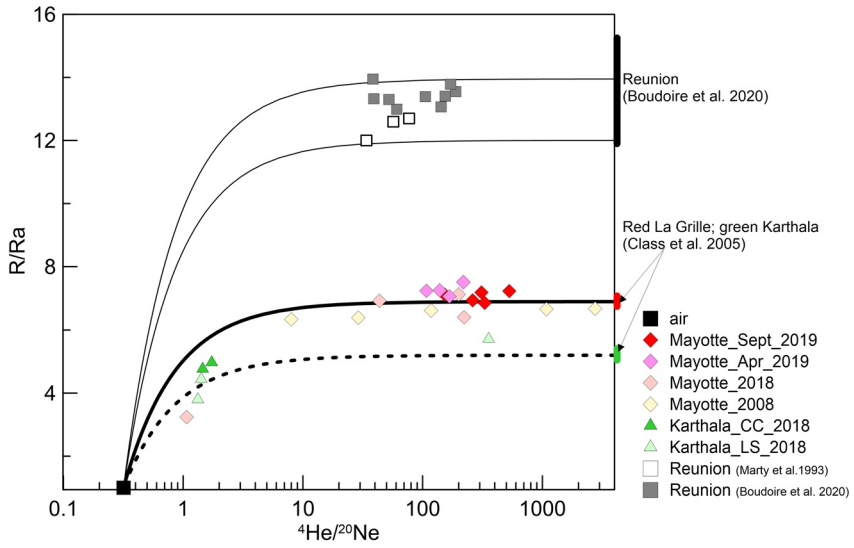

Figure 3. $^{4}He/^{20}Ne$ versus $^{3}He/^{4}He$ (R/Ra) in fumaroles and bubbling gas from Grande Comore and Mayotte. For comparison are shown data from bubbling gases at La Reunion from Boudoire et al., (2020) and Marty et al., (1993). Thick and dash black lines indicating air-magma mixing are calculated from the average value (from Class et al. [2005]) of La Grille and Karthala fluid inclusions respectively. Thin black lines are calculated as the minimum and maximum of bubbling gases at La Reunion. At the right side of the diagram are also indicated three solid black red and green bars, corresponding to the range of the R/Ra variability of La Reunion, La Grille, and Karthala fluid inclusions respectively.

deep plume sources (EMI, HIMU) and a shallower depleted convective ambient mantle or (b) mixing between a homogeneous deep plume sources (EMI component), plus a variable contribution of the shallower heterogeneous and old metasomatized oceanic lithosphere. Whatever the source of the mantle heterogeneities, all authors agree that Karthala lavas and rare old samples from Mayotte record the strongest EM1 contribution of the Comorian plume (Pelleter et al., 2014). According to Class et al. (1998), the alkali basalts of Karthala reflect mainly plume derived melts, while the basanites of La Grille are the products of interaction of plume melts with the metasomatized oceanic lithosphere. Class et al. (2005) show that olivines in Grande Comore lavas span a relatively small range of low-$^{3}He/^{4}He$ compositions. La Grille "lithosphere-dominated" lavas have preserved a nearly MORB signature (6.75–7.08 R_A) suggesting that amphibole forming metasomatism occurred before the arrival of the plume. All samples show good correlations between Sr–Nd–He isotope ratios, indicating that the Grande Comore $^{3}He/^{4}He$ ratios are not significantly influenced by crustal contamination and reflect recent mixing between plume- and lithosphere-derived melts. These authors highlight that the deep plume component has a low and well constrained $^{3}He/^{4}He$ signature of 5.2 ± 0.2 R_A. On the basis of the correlation with Osmium isotopes, Class et al. (2009) argue that the low-He signature does not record contribution from subcontinental lithospheric mantle, but that of a deep plume interacting with oceanic lithosphere. In this frame, the Comoros plume would represent a "low $^{3}He/^{4}He$ – high $^{187}Os/^{186}Os$" hotspot whose deep source is dominated by recycled ^{4}He-rich material.

A detailed treatment of this topic is out of the scope of this paper and will be treated in ongoing studies. Whatever the specific process producing the low-$^{3}He/^{4}He$ signature, we show that Karthala gases record a signature consistent with that recorded in the fluid inclusions of its lavas. On the contrary, Mayotte gases have a slightly higher $^{3}He/^{4}He$ signature, which matches that of La Grille lavas. These findings are consistent with the barometric results of previous works (Bachèlery et al., 2019; Berthod et al., 2020) on the lavas of Mayotte submarine eruption, showing that these evolved basanite magmas are extracted by large shallow mantle reservoirs (50–20 km depth) located between the Moho and the upper oceanic lithosphere.

The $^{4}He/^{40}Ar^{*}$ values measured in Karthala (only one reliable value) and Mayotte gases vary in a narrow range (1.2–1.7), falling within that typical of fertile mantle ($^{4}He/^{40}Ar^{*} = 1–5$; Marty, 2012) and magmatic values from other geodynamic settings (e.g., Boudoire, Rizzo, et al., 2018; Bräuer et al., 2011; Paonita et al., 2012; Rizzo et al., 2019). In magmatic environments, this ratio varies during melts degassing and is indicative of relative entrapment pressures (e.g., Boudoire, Rizzo, et al., 2018; Paonita et al., 2012). Focusing

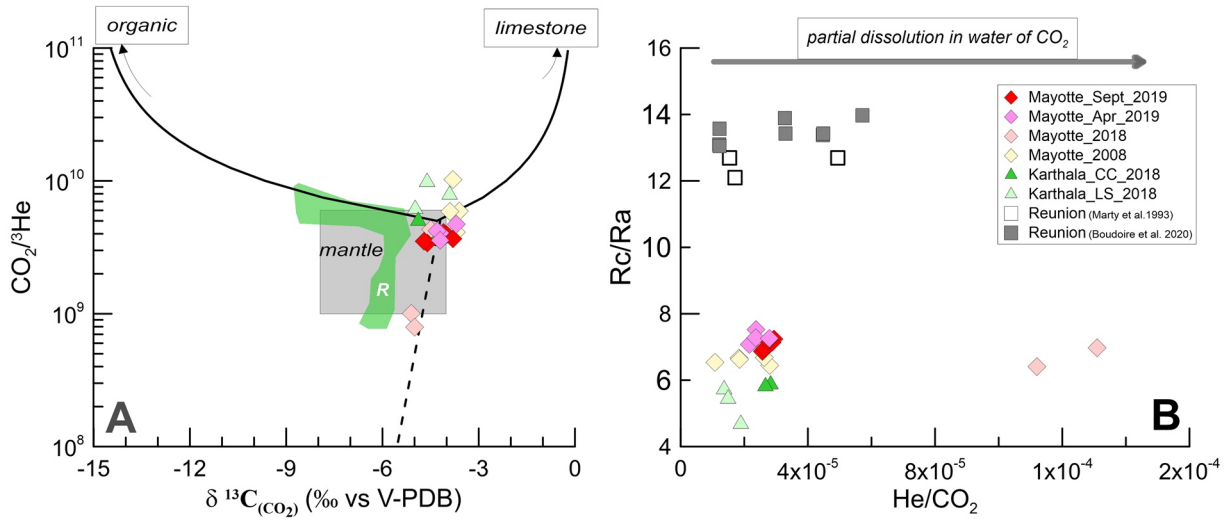

Figure 4. (a) $\delta^{13}C$ of CO_2 versus $CO_2/^3He$ diagram of fumaroles and bubbling gases at Grande Comore and Mayotte. (b) He/CO_2 versus Rc/Ra. For comparison is indicated also the variability of corresponding gases at La Reunion (R). Panel (a) shows that gases at Comore archipelago are in the field of Mantle-like origin with no evident organic or limestone contributions. Solid lines are mixing curves between organic, mantle and limestone endmembers, while the dashed line indicates a Rayleigh fractionation dissolution. Panel (b) displays a variable degree of water-gas interaction affecting CO_2 variability.

on Mayotte gases for which $^4He/^{40}Ar^*$ is available for different gas emissions and surveys dates, we do not notice systematic variations. This leads us to two important deductions: the first is that this ratio is not modified by gas-water interaction as for example, He/CO_2 (see Section 5.2) and thus can be used to track temporal variations eventually related to changes in magmatic dynamics; the second is that Mayotte gas emissions reflect a magmatic degassing occurring in a narrow range of depth. In other words, we could consider a homogeneous (in terms of depth) source of degassing. If we consider the findings of a recent study carried out at La Reunion, in which Boudoire, Rizzo, et al. (2018) constrained a range of $^4He/^{40}Ar^* = 2.1 \pm 0.4$ for fluids exsolved at underplating (10–15 km below Piton de la Fournaise), assuming a comparable ratio in primary magmas below Mayotte, we could speculate that BAS emissions reflect the degassing of a melt ponding at comparable depths. Finally, the lack of evident temporal variations leads us to consider limited depth variations of the melt feeding the discharge of BAS emissions.

5.2. Evidences of Gas-Water Interaction and Origin of CO_2 and CH_4

To evaluate the carbon origin of CO_2 in Karthala and Mayotte gases, $\delta^{13}C$ is diagnostic of the original geochemical environment, being able to discriminate between a magmatic source ($-8‰ < \delta^{13}C < -4‰$; Sano & Marty, 1995), the contribution from subducted marine limestone with $\delta^{13}C = 0‰$, and matter of organic origin with much lighter $\delta^{13}C = -25‰$ (Hoefs, 2015). Thus, we correlated the variation of the $CO_2/^3He$ versus $\delta^{13}C$ ratio based on the approach proposed by Sano and Marty (1995 and references therein). In order to evaluate the secondary processes of gas-water interaction, we have considered data corrected for air only for samples having $N_2 < 22\%$.This is because for samples having $N_2 > 22\%$, the correction would have yielded unrealistic ratios (Table 1). Figure 4a plots two mixing curves modeled considering both an organic and a limestone endmember, in which the mantle corresponds to $CO_2/^3He = 5.0 \times 10^9$ and $\delta^{13}C = -4.4‰$, which result from the average values of our data and data from literature. For both organic and limestone endmembers, a value of $CO_2/^3He = 1.0 \times 10^{13}$ is assumed, whereas for organic and limestone $\delta^{13}C$ endmember is assumed $\delta^{13}C = -25‰$ and $\delta^{13}C = 0‰$, respectively (Sano & Marty, 1995). As known from other studies in hydrothermal gases (Capasso et al., 2005; Gilfillan et al., 2009; Rizzo et al., 2019), the $CO_2/^3He$, He/CO_2, CH_4/CO_2 ratios, and $\delta^{13}C$ isotopic signature can be potentially modified by gas-water interaction in which CO_2 dissolves preferentially with respect to the other species. These effects need to be evaluated and eventually filtered out in order to calculate the thermobarometric conditions of the hydrothermal system feeding the gas seeps (Figures 2 and 4). In Mayotte gases, we observe only a modest variability of the He/CO_2 ratio (Figure 4), which overlaps with that found in Karthala fluids, with the exception of two 2018 samples from

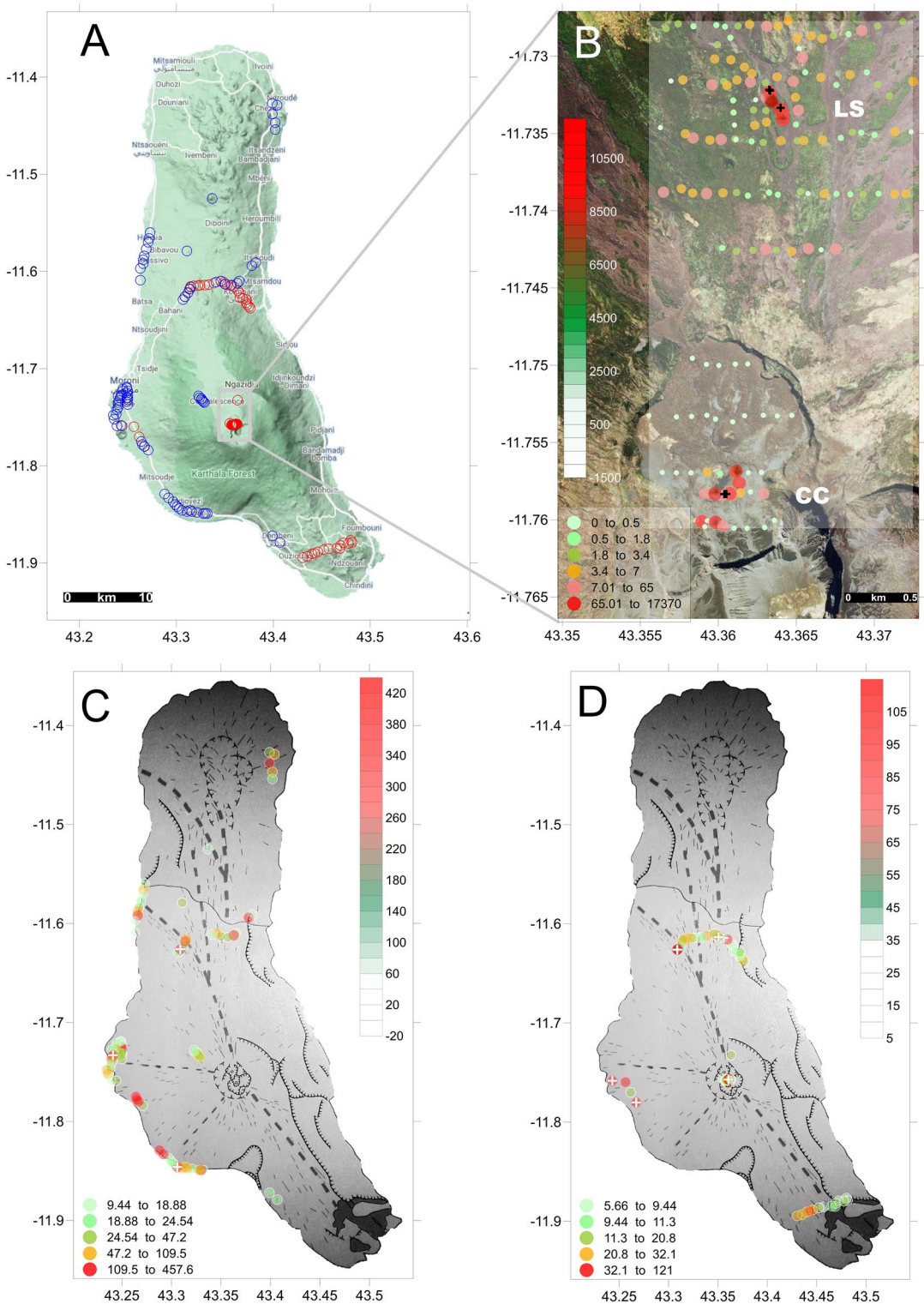
A
B
C
D
LS
CC
0 km 10
0 km 0.5
10500
8500
6500
4500
2500
500
-1500
0 to 0.5
0.5 to 1.8
1.8 to 3.4
3.4 to 7
7.01 to 65
65.01 to 17370
9.44 to 18.88
18.88 to 24.54
24.54 to 47.2
47.2 to 109.5
109.5 to 457.6
5.66 to 9.44
9.44 to 11.3
11.3 to 20.8
20.8 to 32.1
32.1 to 121

Figure 5.

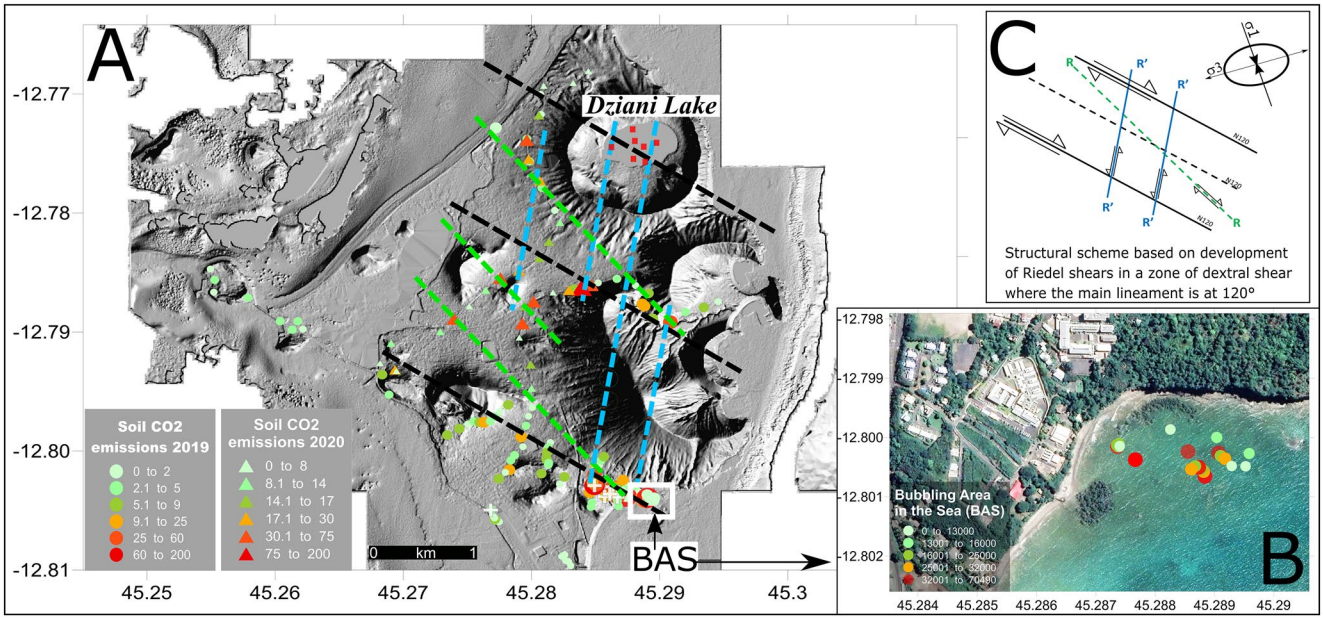

Figure 6. (a) Digital elevation map of Petite Terre highlighting the volcanic cones and the soil CO_2 emissions by a classed post map (where soil CO_2 flux is expressed in range of g m^{-2} d^{-1}) showing 2019 and 2020 surveys. The white crosses are the sites of soil CO_2 sampling for isotopic analysis. The red squares within the Dziani lake are the bubbling sites investigated byMilesi et al. (2020). BAS indicates the bubbling area in the sea, which is magnified in (b) as a classed post map of the CO_2 flux measurements carried out in 2019. The structural trend in (a) is adapted to the Mayotte soil emissions from the theoretical structural scheme exposed in panel (c) based on a dominant shear zone N120°.

the "MAN" pools with low gas flux that show $He/CO_2 > 1.0 \times 10^{-4}$. Similar evidences were observed by BRGM in 2005 samples 9a–c over the whole Mayotte tidal flat (Traineau et al., 2006) and might suggest an increase in gas fluxes after 2005. In order to constrain the pristine C isotopic signature of CO_2 in Karthala and Mayotte, we modeled a Rayleigh fractionation assuming a dissolution under equilibrium conditions based on the approach used in Rizzo et al. (2019). The Clark and Fritz (1997) equation is as follows:

$$\delta^{13}C_{CO_2} = \left(\delta^{13}C_{CO_2}\right)_0 + \varepsilon \ln(f) \quad (5)$$

where the subscript 0 indicates the initial CO_2 isotope composition and f is the fraction of the residual gas phase, while ε is the fractionation factor between DIC (dissolved inorganic carbon) and gaseous CO_2 ($CO_{2,(g)}$). In turn, ε depends on water temperature and pH, which are unknown, therefore, for our purpose the values of temperature and pH has been chosen which better approximate our data set corresponding to $T = 32$°C and pH = 5.71. These values correspond to those measured in the marine water of the Mayotte tidal flat by BRGM surveys (Sanjuan et al., 2008; Traineau et al., 2006). Our results show that Karthala gases are not evidently affected by interaction with shallow waters, as well as most Mayotte bubbling gases record only a minor partial dissolution of CO_2 (Figure S1, where data plotted refer to air-corrected data – Table 1). The modest effect of preferential dissolution of CO_2 in water with respect to CH_4 and He is evident in Figure 4b, where He/CO_2 versus Rc/Ra are shown. Therefore, not considering the samples MAN affected by minor dissolution effects, the general variability of Mayotte and Karthala gases falls well within the range of mantle values (Figure 4a). In spite of streaming through a thick carbonate sequence of the coral reef or of the extensive bacterial contribution recorded in the nearby gas bubbling of the Dziani lake (Milesi et al., 2019, 2020), the gases of Mayotte tidal flat do not show any obvious limestone or organic

Figure 5. Soil CO_2 measurements at Grande Comore. In panel (a) sites of measurements distinct in blue and red for 2017 and 2018 surveys respectively (this study). Inside the white rectangle are indicated the 2018 sites of measurements not indicated in panel (b). In Figure 7b a classed post map (where soil CO_2 flux is expressed in range of g m^{-2} d^{-1}) and a contour plot of soil CO_2 emission of the 2014 survey at the summit of Karthala volcano realized using the accumulation chamber method. CC indicates the Central Caldera area; LS indicates La Sufriere; the sites of the gas sampling of 2018 reported in Table 1 are indicated as black crosses. Figures 7c and 7d are related to 2017–2018 surveys respectively realized using the "dynamic concentration method" (Gurrieri and Valenza [1988]); the white crosses in panels (b and c) are the sites of soil CO_2 sampling for isotopic analysis. On both maps it has overlapped the structural map from Bachèlery and Coudray (1993).

contributions. Their magmatic signature can be constrained at $\delta^{13}C \approx -4.3‰$, which can also represent the magmatic signature of Karthala gases. This statement is supported by the narrow variability of $\delta^{13}C$ range both at Karthala fumaroles ($-4.9‰ \le \delta^{13}C \le -3.9‰$) and Mayotte BAS high flux bubbling pools least affected by gas-water interaction ($-4.9‰ \le \delta^{13}C \le -3.5‰$), as well as by their relatively stability in time considering data from BRGM of 2006 and 2008 campaigns ($-4.3‰ \le \delta^{13}C \le -3.2‰$) as well as in 2016 with $\delta^{13}C = -3.2‰$ (G7 point by Milesi et al. [2020]). Therefore, a $\delta^{13}C \approx -4.3‰ \pm 0.2‰$ is a reasonable approximation of a possible $\delta^{13}C$ magmatic signature for the archipelago.

If compared to the bubbling springs of La Réunion (Figure 4a), we notice that the $\delta^{13}C$ signature of Mayotte and Karthala gases is slightly less negative and shows a minor variability. It is worth noting that La Réunion gases with $\delta^{13}C \approx -6‰$ display a trend of decrease of $CO_2/^3He$ suggesting the occurrence of a process of selective dissolution of CO_2 in water, which is observed in Mayotte only for the samples MAN 1 and 2.

Even if the Karthala and Mayotte fluids are CO_2 dominated, we recall that they show a progressive enrichment in CH_4 up to concentrations of 2,982 ppm in gases from Mayotte, which allowed to measure its isotopic composition of C and H (δD of methane was measured only in DIST-1 and C1-2, Table 1). Following the classification proposed by Schoell (1980) (Figure S2), samples DIST-1 and C1-2 could be considered of abiogenic origin, coherently with the G3 bubbling spot with the highest gas flux in the Dziani lake, recently documented by Milesi et al. (2020). The same authors report of a G7 sample in the BAS area which shows similar $\delta^{13}C$ of DIST-1 and C1-2 but very negative δD of methane (−250‰). However, it must be stressed that distinguishing between methanogenesis processes of biological origin or thermogenic processes at the origin of CH_4 (Mazzini et al., 2011; Schoell, 1980; Welhan, 1988) is complicated by possible mixing between endmembers with different isotopic signature (Taran et al., 2010) or by the occurrence of oxidation processes (e.g., Batista Cruz et al., 2019). It is therefore clear that further data are needed to better constrain the origin of methane in the BAS area of Mayotte.

5.3. CO_2 Degassing From Soil

Volcanic areas are often places where diffuse outgassing of CO_2 emission occurs, facilitated by tectonic structures which locally increase soil permeability. On seismically and volcanically active areas like the Comoros, soil CO_2 emissions have been investigated in order to identify hidden tectonic structures driving fluid emissions to the surface (e.g., Bonforte et al., 2013; Boudoire et al., 2017; Giammanco et al., 2006; Gurrieri et al., 2008; Irwin & Barnes, 1980; Liuzzo et al., 2013). In volcanic tropical settings like the Comoros, the presence of significant fraction of soil CO_2 emissions can also be ascribed to biogenic activity, which may be mixed with gas originating from magmatic sources and whose relative proportion may evolve in time as affected by seasonal effects and the evolution of the seismic and volcanic activity (e.g., Boudoire, Finizola, et al., 2018; Chiodini et al., 2008; Liuzzo et al., 2015).

While rift zones are marked by well defined alignments of volcanic cones in Grande Comore, they are much less defined in Mayotte, where a set of mafic scoria cones and phonolite maars are scattered on the Petite Terre island (Famin et al., 2020; Michon, 2016; Nehlig et al., 2013; Tzevahirtzian et al., 2021). In Grande Comore, volcano flanks are often resurfaced by the frequent emplacement of lava flows, nevertheless thick soils and sand covers are found in most locations, suitable for the measurement of soil CO_2 fluxes. At Petite Terre, the recent explosive activity of phonolitic maars emplaced a widespread cover of several meters thick fine grained ashes that, together with the low altitude of the island and the widespread urban context, limit the areas suitable for CO_2 flux measurements. In our survey strategy, we aimed at characterizing the CO_2 fluxes from the soil on the territory and linking them with known or hidden tectonic structures and with the main degassing areas (summit of Karthala in Grande Comore and Dziani lake and Airport tidal flat in Mayotte). Measurements on Mayotte tidal flat were performed at low tide, when the sandy/muddy flat is wet but without a continuous water cover, excepted some large bubbling pools. Samples of soil gas were taken alongside the soil CO_2 flux measurements to investigate the isotopic signature of carbon in CO_2 and thus constrain the sources of the soil CO_2 emission. As previously mentioned in Section 3.1, as the soil CO_2 data set was acquired using two different methods and at different times, it is not uniform and therefore our choice in data analysis was to consider each area separately. Even if acquired in different seasons and times, all the measurements were carried out on dry sunny days and generally stable weather conditions. Where possible, measurements were performed at a spacing of ca. 50 m or less, though in some cases

distances between individual sites and length and orientation of the tracks were dependent upon local urban density, morphological obstacles, and vegetation cover. Concerning vegetation cover, we point out that in the summit area of Karthala, where the measurements were carried out, vegetation was almost absent. In the peripheral areas of Karthala and at Petite de Terre, the vegetation cover was typically tropical with a prevalence of C_3 type plants (Hoefs, 2015). At the measurement sites, however, the density of the cover was on average low and estimated at about 30% within an average 10 m radius of each measurement and never more than 50%.

5.3.1. Grande Comore

At Grande Comore three campaigns were conducted for the measurement of soil CO_2 using two different methods: (a) accumulation chamber and (b) dynamic concentration (Figure 5).

The first survey at Grande Comore (November 4–8, 2014) was conducted by Benavente and Brotheridge (2015) and focused on exploring the potential geothermal resources of the island. Using the accumulation chamber method (Chiodini et al., 1998), the survey concentrated on the summit area of Karthala volcano, providing a total of 155 measurements of CO_2 flux (Table 2), and only a subset of measurements was performed on the volcano flanks showing very low soil degassing rates. In the summit caldera, the survey by Benavente and Brotheridge (2015) focused on the northern and recently active (2007) part of the caldera, consistently with previous geophysical and CO_2 surveys of Lénat et al. (1998) and Bernabeu et al. (2018), showing that the strongest hydrothermal activity occurs in this area (CC area). In addition, Benavente and Brotheridge (2015) provide the first data set on the most active and high temperature Soufrière area, on the northern rift (LS area). The results of the 2014 survey are plotted in Figure 5b. The soil CO_2 flux ranges from background air (0 flux) up to 17,364 g m^{-2} d^{-1}. The grid of points in the area investigated by Benavente and Brotheridge (2015) was suitable for the estimation of the total budget of CO_2 flux emission at that period, which was calculated by using the GSA method (Chiodini et al., 1998), resulting in an average of ∼291.2 Mg d^{-1} and ∼695.8 Mg d^{-1} at the crater and La Soufrière areas respectively. The remaining summit area investigated of Karthala volcano is characterized by a general very low average of CO_2 flux.

In 2017 (November 28–December 7) and 2018 (October 11–16), the second and the third soil CO_2 measurement surveys were carried out by IPGP and INGV teams, using the dynamic method (Gurrieri & Valenza, 1988) and focusing on the volcano flanks and La Grille area. The unknown k value, necessary for the application of the dynamic method (Equation 2), has been chosen from those which give the minimum percentage deviation between the most probable range of k values in volcanic soils (Camarda et al., 2006a) and in consideration of the similarity with soil CO_2 emission measured at La Reunion (Boudoire et al., 2017; Liuzzo et al., 2015). For all the measurements at Karthala a k value of 30 μm^2 has been chosen (see Table S1). Considering reasonable that the probable range of permeability in volcanic soil ranges between 20 and 40 μm^2, the percentage deviation is less than 6.5% in all the measurements carried out at Karthala.

Eighty-seven measurements were taken during the 2017 campaign in the distal area of the Karthala volcano, with soil CO_2 flux ranging between ∼9 and 450 g m^{-2} d^{-1} (Table 2). During the 2018 campaign, we carried out 65 measurements, where some were partially overlapping the previously surveyed area, however most were in new areas not covered by the 2017 survey (Figure 5a). In 2018, minimum and maximum fluxes are around 5 and 950 g m^{-2} d^{-1} respectively, and confirmed that the maximum fluxes occur inside the summit caldera, close to the CC hot ground and fumarolic field. The findings of these two campaigns (Figures 5c and 5d) show a possible correlation between the main structures (Bachèlery & Coudray, 1993) and the highest flux emissions, confirming that the spatial distribution of the soil CO_2 flux is tightly linked to the tectonic structures of Grande Comore. The Soufrière fumaroles and the maxima on the volcano flank fall on the main rift zones previously identified on the basis of the alignment of volcanic cone. Interestingly, anomalous areas of high CO_2 soil flux extend at low altitude, both in the northern and western part, where a recent seismic and volcanic activity has occurred, while relatively lower fluxes are measured in the southern part of the island, which corresponds to the oldest little active part of Grande Comore (see Bachèlery et al. [2016] for a recent review).

It is interesting to note the similarity in the rate of soil CO_2 flux measured in the Grande Comore with those measured on a tropical island with comparable characteristics, such as La Reunion. In Liuzzo et al. (2015) the soil CO_2 flux documented on the Piton de la Fournaise volcano were in the range of 5.52–701.56 g m^{-2} d^{-1}

and were measured during quiescence phases. In spite of its strong eruption rate, Piton de la Fournaise lacks an area of strong degassing near its summit, which instead occurs on the older and quiescent Piton des Neiges volcano (Boudoire et al., 2020; Marty et al., 1993).

5.3.2. Mayotte – Petite Terre

The occurrence of a widespread ash cover makes the dynamic concentration method not suitable for most CO_2 flux measurements at Petite Terre, Mayotte, where surveys were performed using the accumulation chamber method in 2019 (September 9–13) and in 2020 (November 11) (Figure 6). On this island, a total of 166 measurements of CO_2 flux were taken from the soil and 53 on the tidal flat of the Airport (BAS: bubbling area in the sea Figure 6b). We did not perform a CO_2 survey inside the Dziani crater; however, it represents a target of future investigations. Not surprisingly the strongest CO_2 soil emissions were measured in the Airport tidal flat, where the CO_2-rich bubbling pools are located, with a range of values between 12 and 70,485 g m^{-2} d^{-1}. Peak emissions are thus 4 times higher than those measured at Karthala. The grid of points for this initial exploration did not lend itself to estimating the overall CO_2 flux budget, which will instead be the focus of future investigations. On land, we measured fluxes that span from background levels (corresponding to the air values concentrations) to 173.4 g m^{-2} d^{-1}, being much lower than in the volcano flanks of Karthala or of la Réunion. Our surveys show that at Mayotte the underlying hydrothermal system is the main source of the outgassing of the island and the bubbling area on the tidal flat is an important area of high CO_2 flux. This could arise from a combination of high fluxes focused in two areas (Airport tidal flat and Dziani) and the widespread and poorly permeable fine ash cover on Petite Terre. The possible influence of the ash cover on soil CO_2 fluxes is however not straightforward. At Petite Terre, the thickness of fine ashes increases from west to east and the soil CO_2 fluxes as well, together with the occurrence of the two main areas of gas bubbling, which are located on the eastern side of the island. Even if the on land soil CO_2 emissions are generally modest compared with other sites, their spatial distribution still permits to identify preferential areas of CO_2 emissions on the ground and to discuss their possible link with hidden tectonic structures, not always recognizable with other methods of investigation. Available data sets (Famin et al., 2020; Tzevahirtzian et al., 2021) show that Petite Terre is the tip of a huge and mostly submarine volcanic ridge with a broad regional alignment in the N120° direction, corresponding to the main regional structure of Comoros archipelago and interpreted as a right-lateral shear in the lithosphere (Famin et al., 2020; Michon, 2016). Results from our surveys (Figure 6a) show a distribution of soil CO_2 degassing which might be overlapped to a possible structural scheme in which a system of fractures is determined by a combination of the main structural trends along N120° and a combination of Riedel's structures coherent with the right shear (Figure 6c). In this scheme, the N120° is well correlated to the alignment of Holocene tephritic scoria cones corresponding to the oldest phase of the recent volcanism of Petite Terre (Nehlig et al., 2013). A NNE-SSW (R') trend of soil CO_2 emission is overlapped on the most recent volcanism of the phonolitic maars, where the principal evidence of outgassing is shown by the BAS zone at the feet of the large "Vigie" maar and the bubbling manifestation inside the Dziani lake (Milesi et al., 2020). A possible trend corresponding to R structures is also appreciable in the central area of the island. Even if this first approach proposes an interpretative evaluation of the spatial outgassing distribution, however it must be stressed that future investigations on larger areas are needed to better understand the detailed structural pattern on Mayotte Island.

5.4. Equilibrium Temperature of Hydrothermal Gases

In the previous paragraphs, we have shown that the fumarolic and bubbling gases of Grande Comore and Mayotte have relatively high methane contents with the proportion of methane being highest at Mayotte. We also highlighted the effect on gas chemistry of partial dissolution of CO_2 in water, as well as identified the samples that showed the most evident effects of this process.

Data of CO_2 and CH_4 poorly or not affected by the dissolution of CO_2 in water allowed us to evaluate the possible gas equilibrium conditions among different gas species in hydrothermal environments. In several geothermal systems, the Fischer-Tropsch process has been successfully used to define the origin of methane since the 60s (D'Amore & Panichi, 1980; Hulston & McCabe, 1962). Nowadays an extensive scientific literature exists that explores the conditions of equilibrium among gas species in hydrothermal environments in order to obtain useful geo-indicators for temperature and pressure (Chiodini & Marini, 1998; Fischer

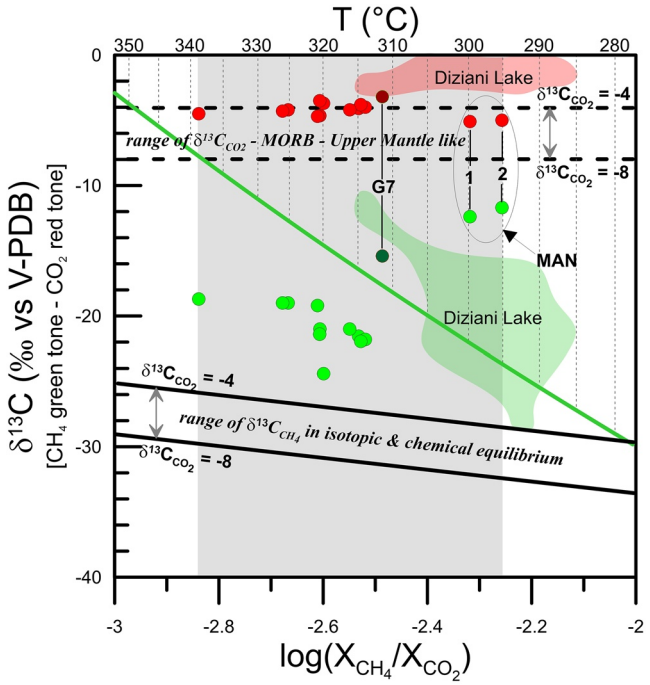

Figure 7. $\delta^{13}C$ for CO_2 (red) and CH_4 (green) versus $\log\left(X_{CH_4} / X_{CO_2}\right)$ of Mayotte bubbling gases. Dark red and green symbols are referred to the G7 sample of Milesi et al. (2020) mentioned in the text, also the red and green area are referred to the variability of the Dziani lake samples from the same authors. The green line correspond to the CH_4 and CO_2 thermal equilibrium expressed in Equation 7 (Giggenbach, 1992), the thick black lines are calculated as Equation 9 for isotopic and chemical equilibrium between CH_4 and CO_2 for two cases of $\delta^{13}C$ (CO_2) corresponding at −4‰ and −8‰ which in turn are indicated as dashed lines.

& Chiodini, 2015). Assuming that in the hydrothermal system an equilibrium is attained between the dominant species H_2O-H_2-CO_2-CO-CH_4, methane can form inorganically from the reaction:

$$CO_2 + 4H_2 = CH_4 + 2H_2O \quad (6)$$

where the formation of methane is favored by the decreasing temperature. For this system we assumed as a condition of thermal equilibrium between CH_4 and CO_2 the equation proposed by Giggenbach (1992):

$$\log\left(X_{CH_4} / X_{CO_2}\right) = 4625 / \left(t_e + 273\right) - 10.4 \quad (7)$$

where t_e is the equilibrium temperature (°C) while X_{CH_4} and X_{CO_2} are the molar fraction of CH_4 and CO_2, respectively.

Under these assumptions, equilibrium temperatures range between around 381 and 460°C at Karthala (Figures S2) which is consistent with data from Benavente and Brotheridge (2015). At Mayotte temperature, vary between 314 and 339°C (excluding MAN 1 and 2 which are recognized as affected by a severe dissolution of CO_2 in water). Interestingly, we do not record a change neither in equilibrium temperature nor in outlet temperature (in equilibrium with sea water temperature) in bubbling gases of the BAS Mayotte tidal flat in the period 2005–2019 in spite of the large magmatic event occurring at ca. 50 km from its coast.

To explore possible evidences of recent input of deep fluids in Mayotte hydrothermal system we evaluated the thermal equilibrium in combination with their isotopic signatures on the basis of their $\delta^{13}C$ isotopic fractionation factor between CO_2 and CH_4. In our BAS samples, $\delta^{13}C_{CH_4}$ ranges from −24.4‰ to −11.7‰, the most positive values corresponding to the MAN samples collected by a low-flux pool close to the mangrove area (Figures S2). To this aim, we have combined the temperatures obtained from (Equation 7) with the temperatures (t_e) calculated using the equation proposed by Bottinga (1969) valid for temperatures ranging between 0 and 700°C:

$$\Delta = 22166 / \left(t_e + 273\right) - 13.8 \quad (8)$$

where Δ is the difference between $\delta^{13}C_{CO_2}$ and $\delta^{13}C_{CH_4}$ values. The relation Equation 8 provides on the whole higher temperatures, ranging between 370 and 515°C (Figures S2), where the samples MAN-1 and MAN-2 – (December 16, 2018), which have been hypothesized to be affected by a strong fluid-water interaction, provide a much higher apparent equilibrium temperature up to 940°C and therefore they are not discussed further.

It is known that temperatures calculated from the CO_2-CH_4 isotopic geothermometer are generally higher than temperatures obtained from geothermometers based on chemical equilibrium (Horita, 2001). This difference is attributable to several process which can affect the final equilibrium and various hypotheses have been invoked to account for outcomes. If external factors able to affect the hydrothermal system cannot be excluded (e.g., an external sources of gas interacting with the hydrothermal system) amongst the causes that might determine discrepancy on the estimation of temperature, a sort of "quenching effect" on the isotopic signature of hydrothermal gases may be considered relevant. Under this assumption, CO_2 and CH_4 were initially in isotopic equilibrium attained at the original source (supposed to be deep) however, during the ascent of the gas to shallow depths, there may not be enough time for the isotopic readjustment thus preserving the original isotope ratios. Such a quenching effect is also justifiable by the faster rate of reequilibration (about 100 times) of the chemical system than the isotopic system (Giggenbach, 1982).

In order to understand if the different temperature obtained by the chemical and isotopic geothermometers could be an expression of a quenching effect acting on the BAS area at Mayotte we plotted the log of the concentration ratio of CH_4 and CO_2 versus the $\delta^{13}C$ of both methane and CO_2 (Ono et al., 1993). In Figure 7 the

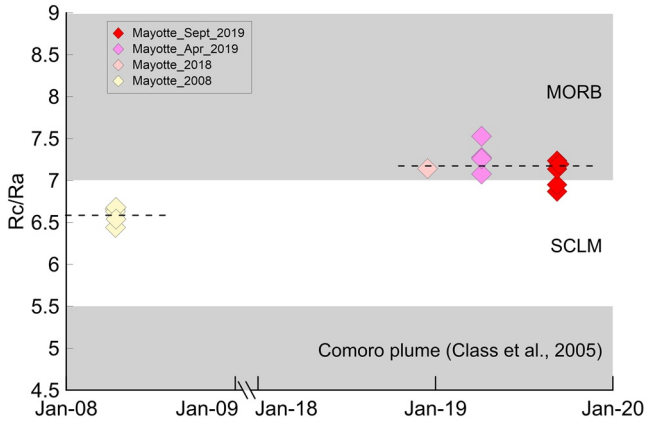

Figure 8. Rc/Ra time series. Rc/Ra has increased by an average 0.5 of between 2008 and 2018–2019. Black dashed lines indicate the averages Rc/Ra for the two distinct periods.

thick black lines were modeled assuming that both chemical and isotopic equilibrium is maintained with a fixed $\delta^{13}C_{CO_2}$ corresponding to the range of magmatic signature, here −4‰ and −8‰ (dashed black lines) by coupling Equations 7 and 8:

$$\log\left(\frac{X_{CH_4}}{X_{CO_2}}\right) = \frac{4625\left(\Delta + 13{,}8\right)}{22166} - 10.4 \quad (9)$$

In addition, the equilibrium temperature calculated using Equation 7 (green line) is shown. The trend of the continuous black lines therefore should represent the variation of the $\delta^{13}C_{CH_4}$ expected if equilibrium conditions are attained by gases injected in the hydrothermal system. However, our data show a significant shift of the methane toward heavier isotopic concentrations. Bacterial oxidation of thermogenic CH_4 can explain isotopic fractionation determining an increase of the isotopic ratio (Baker & Fritz, 1981; Coleman et al., 1981). For instance, this process may be probable in the Dziani lake, where Milesi et al. (2020) have underlined a probable mixing between gas of biogenic and magmatic origin.

Although a carbon isotopic fractionation of methane cannot be excluded, some important differences between the gases of the BAS area and Dziani Lake should be underlined. The range of variability of $\delta^{13}C_{CH_4}$ of the BAS samples is consistent with an abiogenic source (Schoell, 1980). Moreover, the δD values of the samples DIST-1 and C1-2 are −137.8‰ and −118.05‰, respectively, being much higher than the value of G2 (−272‰) methane-rich pool of Dziani lake reported by Milesi et al. (2020), confirming a probable abiotic origin of methane at BAS. Chemical equilibrium temperatures are systematically higher at BAS than at Dziani (<290°C), further suggesting an inorganic origin of BAS methane, or a more magmatic contribution in the hypothesis of a binary mixing between biotic and abiogenic methane. The methane-rich geochemical environment of the Dziani gases is definitely conditioned by the microbial activity in lacustrine waters, very different from the CO_2-rich geochemical environment of the BAS area. It is therefore likely that a quenching effect could explain the shift toward more positive $\delta^{13}C$ values of methane in the BAS data that "freezes" the isotopic equilibrium at corresponding higher temperatures. Assuming that a quenching effect is significant on the BAS samples, the consequences are equally important; under this hypothesis the temperature would have a corresponding isotopic equilibrium in the range estimated by Equation 8, that is between 370 and 515°C and, in turn, such high temperatures can be explained by deep magmatic inputs.

5.5. Temporal Variations of $^3He/^4He$ in Gases From Mayotte

In order to have further evidences of possible variations of geochemical parameters that may have recorded the ongoing submarine volcanic activity, we evaluated the time variation of the helium isotope ratio. This tracer was found to be crucial in defining magmatic recharge in deep reservoirs in many volcanic systems on Earth (Boudoire et al., 2020; Caracausi et al., 2003; Paonita et al., 2016; Rizzo et al., 2015, 2016; Sano et al., 2015). Figure 6 shows values from the 2008 (BRGM repository) and the 2018–2019 surveys. As discussed before, the interpretation of this parameter is quite complex in the Comoros context, because of the possible "low-$^3He/^4He$" signature of the deeper undegassed astenospheric source. Our data suggests that the helium isotopic signature of the BAS fluids (Figure 8) was relatively low in the 2008 samples and it becomes significantly higher (average increase of 0.58 Rc/Ra) in the samples from the 2018 survey. This shift is consistent with the drainage of large volumes of evolved basanite magma from shallow mantle lithospheric depth feeding the Mayotte gaseous emissions at least in 2008, whose potential signature is very close to that recorded by fluid inclusions at La Grille (Class et al., 2005). Since the beginning of the eruption, the Rc/Ra signature of BAS fluids approaches that conventionally accepted for convective MORB mantle (8 ± 1 Ra, Graham, 2002). Thus, we can tentatively speculate that this time evolution is associated with the emplacement of sub-lithospheric magmas at shallower depth along the large Mayotte volcanic ridge.

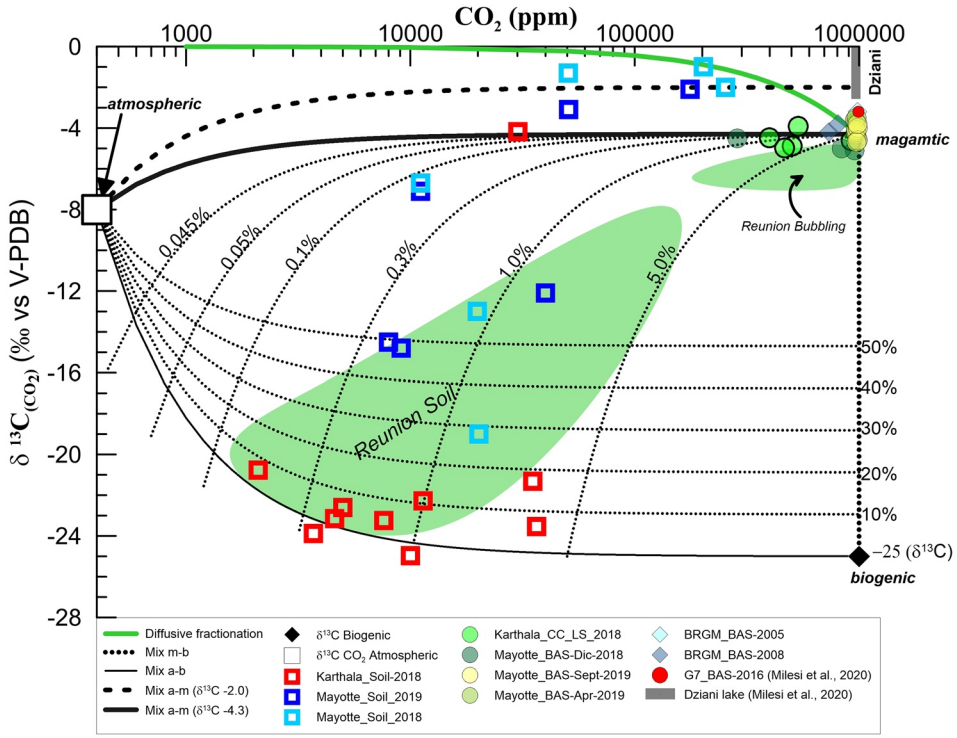

Figure 9. Diagram plotting carbon isotopic composition of soil CO_2 versus soil CO_2 log-concentrations (ppm) showing the theoretical binary mixing curves between three endmembers: atmospheric, biogenic and magmatic. Also shown are the binary mixing curves (hyphen curve) which allow a differentiation in the percentage of the magmatic component (M) in the hypothesis that the biogenic contribution could be extended up to $\delta^{13}C$ 25‰ (Hoefs, 2015). Green areas are referred to La Reunion soil and bubbling gases data repository, while the gray bar is the $\delta^{13}C_{(CO2)}$ Diziani lake's variability from Milesi et al. (2020).

5.6. Gas Emissions From the Soil

Soil CO_2 emission can be ascribed to various origins and generally the total outgassing budget results from a mixture of different sources (Amundson et al., 1998; Cerling et al., 1991; Chiodini et al., 2008; Liuzzo et al., 2015). With the aim at quantifying the different contributions other than those of magmatic origin, such as biogenic source or air contamination in soil CO_2 flux, 22 gas samples were collected at Grande Comore and at Mayotte for CO_2 concentration and carbon isotopic analysis ($\delta^{13}C_{CO_2}$) (Table 1). All the samples were taken directly at 0.5 m depth in the soil, as described in Section 3.2. The results of their CO_2 concentration and C isotopic signature are shown in Figure 9, and are modeled as a mixing of three possible endmembers: atmospheric, biogenic and magmatic. Figure 9 also reports $\delta^{13}C$ of gas from fumarolic fields at Karthala (central crater CC and La Soufrière LS, Figure 5b) and from the bubbling marine area off the coast at Mayotte (BAS, Figure 6b), both obtained from the 2017–2018 surveys. Included in Figure 9 are also data collected at Mayotte by BRGM in 2005–2008 (BRGM/RP-568082 Final reports 2008) and in 2016 from Milesi et al. (2020) at the Dziani volcanic lake, with the exception of sample G7 that was collected in 2016 at the bubbling area BAS. We report the endmembers of atmospheric ($\delta^{13}C = -8‰$) and "biogenic" ($\delta^{13}C = -25‰$; Hoefs, 2015) carbon (corresponding to organic matter). In Figure 9, we report the mixing curves between the three endmembers reported above. The "magmatic" endmember was fixed considering the $\delta^{13}C$ average values of CO_2 of fumarolic and bubbling gases from Karthala and Mayotte, which we considered representative of the magmatic signature beneath these islands of the Comore archipelago ($\delta^{13}C = -4.3‰$). This choice is supported by the small narrow variability of $\delta^{13}C$ range of variation both in at Karthala fumaroles ($-4.9‰ \le \delta^{13}C \le -3.9‰$) and Mayotte BAS high flux bubbling pools least affected by gas-water interaction ($-4.9‰ \le \delta^{13}C \le -3.5‰$, slightly higher values up to 5.7 being those of the MAN low flux pool), and their relatively stability in time considering data from BRGM of 2006 and 2008 campaigns

($-4.3‰ \leq \delta^{13}C \leq -3.2‰$) as well as in 2016 with $\delta^{13}C = -3.2‰$ (G7 point by Milesi et al. [2020]), thus a reasonable approximation of a possible $\delta^{13}C$ magmatic signature for the archipelago.

The Karthala isotopic signature regarding $\delta^{13}C$ in CO_2 from the soil is much wider than in the fumaroles and ranges in the interval $-24.9‰ \leq \delta^{13}C \leq -4.2‰$. Almost all of the isotopic values show a low contribution of magmatic gas and a variable degree of air contamination. A few samples showing high CO_2 concentration have however a modest magmatic contribution (less than 20%) and correspond to sites close to the main structural lineaments showed in Figure 7. The vegetation cover at Karthala, as on all Comorian islands, is essentially tropical and therefore predominantly characterized by C_3 plants. Isotopically, C_3 plants have an isotopic signature which range between −35 and −20 (Hoefs, 2015). Therefore, a possible impact on soil CO_2 could result in generally very negative $\delta^{13}C$ values, which seems significant in the Karthala flanks soil emissions. A single $\delta^{13}C$ value from the soil at Karthala has an isotopic signature close to the magmatic endmember and the corresponding site is very close to the steaming fumarolic field inside the summit CC caldera. These results allow us to conclude that during the 2017 and 2018 surveys, which were performed during a phase of quiescence of the volcano, soil CO_2 emission on the flanks at Grande Comore was predominantly of biogenic origin, while clear evidence of volcanic origin CO_2 emission was detectable only at the summit crater of Karthala. This overall picture of gas fluxes and isotopic signature at Karthala is in strong contrast with that found during a similar quiescence period at Piton de la Fournaise (Liuzzo et al., 2015). On Piton de la Fournaise, only weak emission of low-temperature fluids and low CO_2 fluxes occur in the central summit area during quiescence periods, while diffuse CO_2 emissions with a clear and strong magmatic contribution (up to 60% of the diffuse fluid composition) have been detected along the main rift zones on the flanks of the volcano. On both volcanoes deep fluid percolation is focused on the main rift zones crossing the volcano edifice. However, the much lower rate of volcanic activity and longer quiescence duration at Karthala translates in low soil CO_2 fluxes with a dominant organic signature. The absence of permanent CO_2-rich emissions below the summit area of Piton de la Fournaise has been attributed to the geometry of its deep plumbing system, which is laterally shifted with respect to the central summit area (Liuzzo et al., 2015; Michon, 2016).

At Mayotte the isotopic values of soil gases taken on land are much more scattered than the Karthala data sampled on the volcano flanks. The range of isotopic variation spans the $-19.0‰ \leq \delta^{13}C \leq -1‰$ range at various CO_2 concentrations. Even taking into account a possible impact of the vegetative cover of C_3 plants, the $\delta^{13}C$ results at Mayotte, show a significant magmatic contribution in contrast to the isotopic signature of Karthala soil emissions. It is interesting to notice a scattered distribution similar to that previously reported for $\delta^{13}C$ in soil emission at La Reunion (Boudoire et al., 2017; Liuzzo et al., 2015). The Comoros archipelago is located in the Equatorial rainforest climate zone and La Réunion in a rainy tropical context. Therefore it is reasonable to consider that the soil of these islands is characterized by similar pedogenesis and biogenic processes to those identified in other tropical zones (Basile-Doelsch et al., 2005; Frank et al., 2002, 2006; Rouff et al., 2012), which in turn can significantly affect the isotopic signature of carbon in soil CO_2, as reported at La Reunion by Liuzzo et al. (2015). It is therefore not surprising that $\delta^{13}C$ of CO_2 distribution in Mayotte lies within a comparable range of values as those reported for isotopic soil CO_2 measurements at La Reunion in previous works (Boudoire et al., 2017; Liuzzo et al., 2015).

The less negative $\delta^{13}C$ values ($-3‰ < \delta^{13}C < -1‰$) were recorded at several soil CO_2 sampling areas that were taken on the beach or on a cliff very close to the BAS bubbling zone. However, these values cannot be explained as a mixing of atmospheric and magmatic CO_2 fixed at −4.3‰. The less negative $\delta^{13}C$ values for these two sites elicit three possible hypotheses: either (a) they may lie in a mixing curve between atmospheric and magmatic endmember where the magmatic signature is more positive (around $\delta^{13}C = -2‰$); (b) they can be affected by isotopic fractionation on the aquifer; or (c) they are affected by kinetic fractionation due to a process of CO_2 diffusion through the soil as observed in other studies (Capasso et al., 2001; Cerling, 1984; Hesterberg & Siegenthaler, 1991; Severinghaus et al., 1996). We stress that we identify this process only in a limited area, very close to the BAS tidal flat, which is affected by a process determining a significant modification of the isotopic signature that ends with less negative $\delta^{13}C$ value. Regarding the first hypothesis, a mixing curve between air and magmatic endmember fixed at $\delta^{13}C = -2‰$ seems to correlate well to these more positive isotopic data (black dashed curve in Figure 9). In addition, the mixing curve at $\delta^{13}C = -2‰$ lies in the range of isotopic signatures of Dziani lake (Milesi et al., 2020). However, Dziani

lake lies within a closed volcanic crater that receives a significant volcanic CO_2 contribution. According to Milesi et al. (2019) also in such lacustrine site biogenic and microbial methanogenesis CO_2 reduction is particularly significant (thus potentially affecting the isotopic signature of CO_2 shifting $\delta^{13}C$ toward more positive signature). These microbial processes have not been identified in our beach context. The similarity of the $\delta^{13}C$ signature between Dziani lake and these few ground sites discussed is unrealistic also because the mentioned soil degassing area is far from Dziani lake, while instead very close to the BAS (a few tens of meters). As a consequence, we should expect an isotopic signature closer to that measured in BAS fluids. Moreover, it is difficult to explain alongside the entire data set presented here, especially considering that the Karthala data fall within a range comparable to the bubbling data at Petite Terre. The second hypothesis invokes an isotopic fractionation that may be ascribed to the interference with the (salty) aquifer, which in turn should determine more negative isotopic values. In addition, the composition of soil gas samples collected at Mayotte do not show detectable CO_2 dissolution in water (see Figure S1), therefore the interference of the aquifer at this site seems to be very modest. Regarding the third hypothesis, a curve of diffusive fractionation was modeled (green line in Figure 9) following Capasso et al. (2001):

$$\delta_i = -\Delta x \cdot \left(\frac{D_{j-a}}{D_{i-a}} - 1 \right) \cdot 10^3‰ \quad (10)$$

where δ_i is the expected fractionated isotopic value of soil CO_2 sample; Δ_x is the variable molar fraction between CO_2 in air and in the sample; D is the binary diffusion coefficient of CO_2 in air; where specifically, D_j is related to ^{12}C, and D_i is related to ^{13}C. In our case, the diffusivity ratio of carbon in CO_2 (by the way D_{j-a}/D_{i-a}) is equal to 1.0044 (from Reid et al., 1977). For these samples, which were collected in the area close to the bubbling zone, it is therefore reasonable to consider a variable grade of isotopic diffusive fractionation that modified gases with a starting isotopic signature probably close to the bubbling gas thus leading to the conclusion that a kinetic diffusive fractionation might be the main process acting in this specific zone of the island.

We are aware that a wider data set would certainly contribute to a more comprehensive understanding of the various processes responsible of the isotopic signature in soil CO_2 gas at Petite Terre. We however underline that the most significant results from this data set support the hypothesis of a clear fingerprint of an active magmatic source into soil CO_2 emissions which has not been clearly identified on the volcano flanks of Karthala. Consequently, we conclude that the high CO_2 fluxes from the BAS tidal area and the time evolution of their He isotopic signature, together with the stronger magmatic CO_2 contribution emissions diffused on land at Petite Terre, potentially record the large magmatic and volcanic event occurring on the submarine flanks of the island. On the contrary, we can anticipate that the future reactivation of Karthala volcano should be recorded by a significant change in CO_2 emissions from the soil in terms of both fluxes, areal distribution and isotopic composition, as observed on other active volcanoes (Liuzzo et al., 2013).

6. Conclusion

This work presents the results of recent campaigns for the measurement of soil, fumarolic and bubbling gas emissions in two islands within the Comoros archipelago: Grande Comore and Mayotte. Although the measurement campaigns of soil CO_2 emissions are not exhaustive for the entire territory of these two islands, the first results show that they are spatially distributed along the main structural features of both Grande Comore and Petite Terre. A significant difference is found in the origin of the CO_2 emitted from the soil. The carbon isotopic signature of soil CO_2 emissions highlights evidence of a low magmatic contribution at distal areas of Karthala volcano, and a significantly higher magmatic contribution in CO_2 emissions at Petite Terre.

Gas geochemistry of fumarolic fields at Karthala (Grande Comore), and bubbling gases at Mayotte fall within the typical range of MORB-type mantle source. Compared with La Reunion data set (Boudoire, Finizola, et al., 2018; Boudoire, Rizzo, et al., 2018; Liuzzo et al., 2015), the Comoros islands data set shows a CH_4 enrichment, and a variable degree of air contamination.

The isotopic signature of helium ($^3He/^4He$) in gas emissions confirms relatively low Rc/Ra values (4.18–7.53) for the entire archipelago compared to other volcanic systems in the Indian Ocean such as Reunion

(12–14.6). $^{3}He/^{4}He$ data are consistent with average values of fluid inclusions for both Karthala and Petite Terre, spanning in the interval of $6.41 \leq Rc/Ra \leq 7.53$ at Petite Terre and $4.68 \leq Rc/Ra \leq 5.87$ at Karthala. The origin of CO_2 in the fumarolic emissions is basically magmatic (−5.7; −3.2) with no evidence of significant organic or sedimentary contribution for both Grande Comore and Mayotte.

Based on the CO_2, H_2, H_2O, and CH_4 contents, a hydrothermal system below Mayotte has been recognized with an equilibrium temperature of ∼300°C. Water-gas interaction process has been detected in Mayotte resulting in a partial CO_2 dissolution in water. The methane of the hydrothermal system seems to be abiogenic in origin.

The differences recognized between Grande Comore and Mayotte may be ascribed to the different states of volcanic activity at the two islands at the time of the surveys. Soil CO_2 emissions at Grande Comore are generally dominated by biogenic origin while there is a clear magmatic CO_2 contribution in Petite Terre.

Moreover, the increased value of Rc/Ra between 2008 and 2018–19 at Mayotte coupled to a not fully reached isotopic equilibrium of the pair $\delta^{13}C_{CO_2} - \delta^{13}C_{CH_4}$ in the hydrothermal fluids may be ascribed to the recent volcanic activity which generated the new submarine volcano 45 km offshore from Petite Terre.

Further investigations and a suitable geochemical monitoring program are needed to better understand the complex volcanic system of Comoros archipelago. Nevertheless, our results show some clues of a potential volcano activity of Mayotte which opens important scenarios for the implication regarding procedures aimed to reduce volcanic hazard in this region.

Data Availability Statement

All data used in this work are included in Tables 1 and 2 and stored in the Earth-prints repository: http://hdl.handle.net/2122/14788.

Acknowledgments
This work is part of the PhD (XXXIV cycle) of Marco Liuzzo at the University of Ferrara. The work has been partially funded by INGV (GECO project Fondi Ricerca libera 2019 INGV) and by REVOSIMA Initiative (IPGP, CNRS, BRGM, and IFREMER) for fieldwork and analytical activities. The authors are grateful to CNDRS of Moroni for the local assistance to our team, as well as thankful to the Interreg Hatari support to A. Di Muro and B. Shafik. The authors are very thankful to P. Allard for lending us the accumulation chamber for soil CO_2 surveys and C. Ventura Bordenga for his invaluable support on the Karthala field. The authors also thank INGV, Sezione di Palermo, for allowing the access to the analytical facilities. In particular, the authors are grateful to S. Cappuzzo who provided some of the technical equipment, F. Salerno and M. Longo for performing analyses of gases chemistry, M. Tantillo and M. Misseri for carrying out the noble gases isotopic measurements in the laboratory, G. Capasso, Y. Oliveri, and A. Sollami for providing CO_2 and CH_4 isotopic analysis in the stable isotopes laboratory. Open Access Funding provided by Istituto Nazionale di Geofisica e Vulcanologia within the CRUI-CARE Agreement.

References

Amundson, R., Stern, L., Baisden, T., & Wang, Y. (1998). The isotopic composition of soil and soil-respired CO_2. *Geoderma*, *82*, 83–114. https://doi.org/10.1016/s0016-7061(97)00098-0

Bachèlery, P., Berthod, C., Di Muro, A., Gurioli, L., Besson, P., Caron, B., et al. (2019). Petrological and geochemical characterization of the lava from the 2018–2019 Mayotte eruption: First results. AGU Fall Meeting Abstracts (Vol. 2019, pp. V52D–06).

Bachèlery, P., & Coudray, J. (1993). *Carte volcano-tectonique (1/50000e) de la Grande Comore et notice explicative*. The French Embassy in Moroni, Comoros, and The University of La Réunion, St. Denis de La Réunion.

Bachèlery, P., & Hémond, C. (2016). Geochemical and petrological aspects of Karthala volcano. In P. Bachèlery, J.-F. Lénat, A. Di Muro, & L. Michon (Eds.), *Active volcanoes of the Southwest Indian Ocean: Piton de La Fournaise and Karthala* (pp. 367–384). Springer-Verlag, Berlin and Heidelberg. https://doi.org/10.1007/978-3-642-31395-0_23

Bachèlery, P., Morin, J., Villeneuve, N., Soulé, H., Nassor, H., & Radadi Ali, A. (2016). Structure and eruptive history of Karthala volcano. In P. Bachèlery, J.-F. Lénat, A. Di Muro, & L. Michon (Eds.), *Active volcanoes of the Southwest Indian Ocean: Piton de La Fournaise and Karthala* (pp. 345–366). Springer-Verlag, Berlin and Heidelberg. https://doi.org/10.1007/978-3-642-31395-0_22

Baker, J. F., & Fritz, P. (1981). Carbon isotope fractionation during microbial methane oxidation. *Nature*, *293*, 289–291.

Basile-Doelsch, I., Amundson, R., Stone, W. E. E., Masiello, C. A., Bottero, J. Y., Colin, F., et al. (2005). Mineralogical control of organic carbon dynamics in a volcanic ash soil on La Reunion. *European Journal of Soil Science*, *56*(6), 689–703. https://doi.org/10.1111/j.1365-2389.2005.00703.x

Bassias, Y., & Leclaire, L. (1990). The Davie Ridge in the Mozambique Channel: Crystalline basement and intraplate magmatism. *Neues Jahrbuch für Geologie und Paläontologie*, *4*, 67–90. https://doi.org/10.1127/njgpm/1990/1990/67

Batista Cruz, R. Y., Rizzo, A. L., Grassa, F., Bernard Romero, R., González Fernández, A., Kretzschmar, T. G., & Gómez-Arias, E. (2019). Mantle degassing through continental crust triggered by active faults: The case of the Baja California Peninsula, Mexico. *Geochemistry, Geophysics, Geosystems*, *20*, 1912–1936. https://doi.org/10.1029/2018GC007987

Benavente, O., & Brotheridge, J. (2015). Comoros surface exploration. *Geochemistry, soil CO_2 flux and shallow temperature surveys* (p. 65). New Zealand Ministry of Foreign Affairs and Trade (MFAT).

Bernabeu, N., Finizola, A., Smutek, C., Saramito, P., & Delcher, E. (2018). Spatio-temporal evolution of temperature and fluid flow through a new "thermo-lithological" boundary; the case of a pit crater of Karthala volcano (Comoros archipelago) refilled on January 13th 2007 by a lava flow. *Journal of Volcanology and Geothermal Research*, *367*, 7–19. https://doi.org/10.1016/j.jvolgeores.2018.10.013

Berthod, C., Médard, E., Bachèlery, P., Gurioli, L., Di Muro, A., Peltier, A., et al. (2020). The 2018-ongoing Mayotte submarine eruption: Magma migration imaged by petrological monitoring. *AGU Fall Meeting, 1–17 December, 2020*.

Bonforte, A., Federico, C., Giammanco, S., Guglielmino, F., Liuzzo, M., & Neri, M. (2013). Soil gases and SAR measurements reveal hidden faults on the sliding flank of Mt. Etna (Italy). *Journal of Volcanology and Geothermal Research*, *251*, 27–40. https://doi.org/10.1016/j.jvolgeores.2012.08.010

Bottinga, Y. (1969). Calculated fractionation factors for carbon and hydrogen isotope exchange in the system calcite-carbon dioxide-graphite-methane hydrogen-water vapor. *Geochimica et Cosmochimica Acta*, *33*, 49–64. https://doi.org/10.1016/0016-7037(69)90092-1

Boudoire, G., Finizola, A., Di Muro, A., Peltier, A., Liuzzo, M., Grassa, F., et al. (2018). Small-scale spatial variability of soil CO_2 flux: Implication for monitoring strategy. *Journal of Volcanology and Geothermal Research*, *366*, 13–26. https://doi.org/10.1016/j.jvolgeores.2018.10.001

Boudoire, G., Liuzzo, M., Di Muro, A., Ferrazzini, V., Michon, L., Grassa, F., et al. (2017). Investigating the deepest part of a volcano plumbing system: Evidence for an active magma path below the western flank of Piton de la Fournaise (La Reunion Island). *Journal of Volcanology and Geothermal Research*, *341*, 193–207. https://doi.org/10.1016/j.jvolgeores.2017.05.026

Boudoire, G., Rizzo, A. L., Arienzo, I., & Di Muro, A. (2020). Paroxysmal eruptions tracked by variations of helium isotopes: Inferences from Piton de la Fournaise (La Réunion island). *Scientific Reports*, *10*, 9809. https://doi.org/10.1038/s41598-020-66260-x

Boudoire, G., Rizzo, A. L., Di Muro, A., Grassa, F., & Liuzzo, M. (2018). Extensive CO_2 degassing in the upper mantle beneath oceanic basaltic volcanoes: First insights from Piton de la Fournaise volcano (La Réunion Island). *Geochimica et Cosmochimica Acta*, *235*, 376–401. https://doi.org/10.1016/j.gca.2018.06.004

Bräuer, K., Kämpf, H., Koch, U., & Strauch, G. (2011). Monthly monitoring of gas and isotope compositions in the free gas phase at degassing locations close to the Nový Kostel focal zone in the western Eger Rift, Czech Republic. *Chemical Geology*, *290*, 163–176. https://doi.org/10.1016/j.chemgeo.2011.09.012

BRGM/RP-568082 Final reports. (2008). Sanjuan, B., Baltassat, J. F. – Estimation du potentiel géothermique de Mayotte: Phase 2 – Etape 2. Investigations.-M., Bezelgues S., Brach M., Girard J.-F., Mathieu géologiques, géochimiques et géophysiques complémentaires, synthèse des résultats.

Cadeau, P., Jézéquel, D., Leboulanger, C., Fouilland, É., Le Floc'h, E., Chaduteau, C., et al. (2020). Carbon isotope evidence for large methane emissions to the Proterozoic atmosphere. *Scientific Reports*, *10*, 18186. https://doi.org/10.1038/s41598-020-75100-x

Camarda, M., Gurrieri, S., & Valenza, M. (2006a). CO_2 flux measurements in volcanic areas using the dynamic concentration method: Influence of soil permeability. *Journal of Geophysical Research*, *111*(B5). https://doi.org/10.1029/2005JB003898

Camarda, M., Gurrieri, S., & Valenza, M. (2006b). In situ permeability measurements based on a radial gas advection model: Relationships between soil permeability and diffuse CO_2 degassing in volcanic areas. *Pure and Applied Geophysics*, *163*(4), 897–914. https://doi.org/10.1007/s00024-006-0045-y

Capasso, G., Carapezza, M. L., Federico, C., Inguaggiato, S. & Rizzo, A. (2005). Geochemical variations in fluids from Stromboli volcano (Italy): Early evidences of magma ascent during 2002–2003 eruption. *Bulletin of Volcanology*, *68*, 897–914. https://doi.org/10.1007/s00445-005-0427-5

Capasso, G., D'Alessandro, W., Favara, R., Inguaggiato, S., & Parello, F. (2001). Kinetic isotope fractionation of CO2 carbon due to diffusion processes through the soil. *Water-Rock Interaction*, *10*, 1497–1499.

Caracausi, A., Italiano, F., Paonita, A., Rizzo, A., & Nuccio, P. M. (2003). Evidence of deep magma degassing and ascent by geochemistry of peripheral gas emissions at Mount Etna (Italy): Assessment of the magmatic reservoir pressure. *Journal of Geophysical Research*, *108*(B10), 2463. https://doi.org/10.1029/2002JB002095

Cerling, T. E. (1984). The stable isotopic composition of modern soil carbonate and its relationship to climate. *Earth and Planetary Science Letters*, *71*(2), 229–240. https://doi.org/10.1016/0012-821x(84)90089-x

Cerling, T. E., Solomon, D. K., Quade, J., & Bowman, J. R. (1991). On the isotopic composition of carbon in soil carbon dioxide. *Geochimica et Cosmochimica Acta*, *55*, 3403–3405. https://doi.org/10.1016/0016-7037(91)90498-t

Cesca, S., Letort, J., Razafindrakoto, H. N., Heimann, S., Rivalta, E., Isken, M. P., et al. (2020). Drainage of a deep magma reservoir near Mayotte inferred from seismicity and deformation. *Nature Geoscience*, *13*(1), 87–93. https://doi.org/10.1038/s41561-019-0505-5

Chaheire, M., Chamassi, M., & Houmadi, N. (2016). Geothermal development in the Comoros and results of geothermal surface exploration. In *Proceedings, 6th African Rift Geothermal Conference Addis Ababa, Ethiopia, 2nd–4th November 2016*.

Chiodini, G., Caliro, S., Cardellini, C., Avino, R., Granieri, D., & Schmidt, A. (2008). Carbon isotopic composition of soil CO_2 efflux, a powerful method to discriminate different sources feeding soil CO_2 degassing in volcanic-hydrothermal areas. *Earth and Planetary Science Letters*, *274*(3–4), 372–379. https://doi.org/10.1016/j.epsl.2008.07.051

Chiodini, G., Cioni, R., Guidi, M., Marini, L., & Raco, B. (1998). Soil CO_2 flux measurements in volcanic and geothermal areas. *Applied Geochemistry*, *13*, 534–552. https://doi.org/10.1016/s0883-2927(97)00076-0

Chiodini, G., & Marini, L. (1998). Hydrothermal gas equilibria: The H_2O-H_2-CO_2-CO-CH_4 system. *Geochimica et Cosmochimica Acta*, *62*, 2673–2687. https://doi.org/10.1016/s0016-7037(98)00181-1

Clark, I. D., & Fritz, P. (1997). *Environmental isotopes in hydrogeology* (p. 328). CRC Press.

Class, C., & Goldstein, S. L. (1997). Plume-lithosphere interactions in the ocean basins: Constraints from the source mineralogy. *Earth and Planetary Science Letters*, *150*, 245–260. https://doi.org/10.1016/s0012-821x(97)00089-7

Class, C., Goldstein, S. L., Altherr, R., & Bachèlery, P. (1998). The process of plume—Lithosphere interactions in the Ocean Basins—The case of Grande Comore. *Journal of Petrology*, *39*(5), 881–903. https://doi.org/10.1093/petroj/39.5.881

Class, C., Goldstein, S. L., & Shirey, S. B. (2009). Osmium in Grande Comore lavas: A new extreme among a spectrum of EM-type mantle endmembers. *Earth and Planetary Science Letters*, *284*, 219–227. https://doi.org/10.1016/j.epsl.2009.04.031

Class, C., Goldstein, S. L., Stute, M., Kurz, MD., & Schlosser, P. (2005). Grand Comore Island: A well-constrained "low 3He/4He". *Earth and Planetary Science Letters*, *233*, 391–409. https://doi.org/10.1016/j.epsl.2005.02.029

Claude-Ivanaj, C., Bourdon, B., & Allègre, C. J. (1998). Ra-Th-Sr isotope systematic in Grande Comore Island: A case study of plume-lithosphere interaction. *Earth and Planetary Science Letters*, *164*, 99–117. https://doi.org/10.1016/s0012-821x(98)00195-2

Coffin, M. F., Rabinowitz, P. D., & Houtz, R. E. (1986). Crustal structure in the western Somali Basin. *Geophysical Journal International*, *86*(2), 331–369. https://doi.org/10.1111/j.1365-246x.1986.tb03832.x

Coleman, D. D., Risatti, J. B., & Schoell, M. (1981). Fractionation of carbon and hydrocarbon isotopes by methane-oxidizing bacteria. *Geochimica et Cosmochimica Acta*, *45*, 1033–1037. https://doi.org/10.1016/0016-7037(81)90129-0

Coltorti, M., Bonadiman, C., Hinton, RW., Siena, F., & Upton, B. G. J. (1999). Carbonatite metasomatism of the oceanic upper mantle: Evidence from clinopyroxenes and glasses in ultramafic xenoliths of Grande Comore, Indian Ocean. *Journal of Petrology*, *40*, 133–165. https://doi.org/10.1093/petroj/40.1.133

D'Amore, F., & Panichi, C. (1980). Evaluation of deep temperature of hydrothermal systems by a new gas geothermometer. *Geochimica et Cosmochimica Acta*, *44*, 549–556. https://doi.org/10.1016/0016-7037(80)90051-4

Deniel, C. (1998). Geochemical and isotopic (Sr, Nd, Pb) evidence for plume-lithosphere interactions in the genesis of Grande Comore magmas (Indian Ocean). *Chemical Geology*, *144*, 281–303. https://doi.org/10.1016/S0009-2541(97)00139-3

Emerick, C. M., & Duncan, R. A. (1982). Age progressive volcanism in the Comoros archipelago, eastern Indian Ocean and implications for Somali plate tectonics. *Earth and Planetary Science Letters*, *60*(3), 415–428. https://doi.org/10.1016/0012-821x(82)90077-2

Evans, W. C., Sorey, M. L., Kennedy, B. M., Stonestrom, D. A., Rogie, J. D., & Shuster, D. L. (2001). High CO_2 emissions through porous media: Transport mechanisms and implications for flux measurement and fractionation. *Chemical Geology*, *177*(1–2), 15–29. https://doi.org/10.1016/S0009-2541(00)00379-X

Famin, V., Michon, L., & Bourhane, A. (2020). The Comoros archipelago: A right-lateral transform boundary between the Somalia and Lwandle plates. *Tectonophysics*, *789*, 228539. https://doi.org/10.1016/j.tecto.2020.228539

Feuillet, N., Jorry, S., Crawford, W. C., Deplus, C., Thinon, I., Jacques, E., et al. (2019). Birth of a large volcano offshore Mayotte through lithosphere-scale rifting. In *Proceedings of the AGU Fall Meeting 2019*. AGU.

Fischer, T. P., & Chiodini, G. (2015). Volcanic, magmatic and hydrothermal gases. In The encyclopedia of volcanoes (2nd ed., pp. 779–797). Academic Press, Elsevier. https://doi.org/10.1016/B978-0-12-385938-9.00045-6

Frank, A. B., Liebig, M. A., & Hanson, J. D. (2002). Soil carbon dioxide fluxes in northern semiarid grasslands. *Soil Biology and Biochemistry*, *34*, 1235–1241. https://doi.org/10.1016/s0038-0717(02)00062-7

Frank, A. B., Liebig, M. A., & Tanaka, D. L. (2006). Management effects on soil CO_2 efflux in northern semiarid grassland and cropland. *Soil and Tillage Research*, *89*, 78–85. https://doi.org/10.1016/j.still.2005.06.009

French, S. W., & Romanowicz, B. (2015). Broad plumes rooted at the base of the Earth's mantle beneath major hotspots. *Nature*, *525*(7567), 95–99. https://doi.org/10.1038/nature14876

Gaina, C., Torsvik, T. H., van Hinsbergen, D. J. J., Medvedev, S., Werner, S. C., & Labails, C. (2013). The African Plate: A history of oceanic crust accretion and subduction since the Jurassic. *Tectonophysics*, *604*, 4–25. https://doi.org/10.1016/j.tecto.2013.05.037

Gérard, E., De Goeyse, S., Hugoni, M., Agogué, H., Richard, L., Milesi, V., et al. (2018). Key role of alphaproteobacteria and cyanobacteria in the formation of stromatolites of Lake Dziani Dzaha (Mayotte, Western Indian Ocean). *Frontiers in Microbiology*, *9*, 796. https://doi.org/10.3389/fmicb.2018.00796

Giammanco, S., Gurrieri, S., & Valenza, M. (2006). Fault controlled soil CO_2 degassing and shallow magma bodies: Summit and lower east rift of Kilauea volcano (Hawaii), 1997. *Pure and Applied Geophysics*, *163*(4), 853–867. https://doi.org/10.1007/s00024-006-0039-9

Giggenbach, W. F. (1982). Carbon-13 exchange between CO_2 and CH_4 under geothermal conditions. *Geochimica et Cosmochimica Acta*, *46*, 159–165. https://doi.org/10.1016/0016-7037(82)90243-5

Giggenbach, W. F. (1992). Chemical techniques in geothermal exploration. Applications of geochemistry in geothermal reservoir development. In F. D'Amore (Ed.), UNITAR/UNDP Centre on Small Energy Resources (pp. 119–143).

Giggenbach, W. F., & Goguel, R. L. (1989). Methods for the collection and analysis of geothermal and volcanic water and gas samples (Vol. 2387, p. 53). New Zealand Department of Scientific and Industrial Research, Chemistry Division Report.

Gilfillan, S., Lollar, B., Holland, G., Blagburn, D., Stevens, S., Schoell, M., et al. (2009). Solubility trapping in formation water as dominant CO_2 sink in natural gas fields. *Nature*, *458*, 614–618. https://doi.org/10.1038/nature07852

Graham, D. W. (2002). Noble gas isotope geochemistry of mid-ocean and ocean island basalts: Characterization of mantle source reservoirs. *Reviews in Mineralogy and Geochemistry*, *47*, 247–317. https://doi.org/10.2138/rmg.2002.47.8

Gurrieri, S., Liuzzo, M., & Giudice, G. (2008). Continuous monitoring of soil CO_2 flux on Mt. Etna: The 2004–2005 eruption and the role of regional tectonics and volcano tectonics. *Journal of Geophysical Research*, *113*(B9). https://doi.org/10.1029/2007JB005003

Gurrieri, S., & Valenza, M. (1988). Gas transport in natural porous mediums: A method for measuring CO_2 flows from the ground in volcanic and geothermal areas. *Rendiconti della Societa Italiana di Mineralogia e Petrologia*, *43*, 1151–1158.

Hajash, A., & Armstrong, R. L. (1972). Paleomagnetic and radiometric evidence for the age of the Comoros Islands, West Central Indian Ocean. *Earth and Planetary Science Letters*, *16*, 231–236. https://doi.org/10.1016/0012-821x(72)90195-1

Hesterberg, R., & Siegenthaler, U. (1991). Production and stable isotopic composition of CO_2 in a soil near Bern. *Switzerland Tellus*, *43B*, 197–205. https://doi.org/10.3402/tellusb.v43i2.15264

Hilton, D. R., Halldórsson, S. A., Barry, P. H., Fischer, T. P., De Moor, J. M., Ramirez, C. J., et al. (2011). Helium isotopes at Rungwe Volcanic Province, Tanzania, and the origin of East African plateaux. *Geophysical Research Letters*, *38*(21). https://doi.org/10.1029/2011GL049589

Hoefs, J. (2015). *Stable isotope geochemistry* (7th ed., p. 208). Springer International Publishing Switzerland. https://doi.org/10.1007/978-3-319-19716-6

Horita, J. (2001). Carbon isotope exchange in the system CO_2-CH_4 at elevated temperatures. *Geochimica et Cosmochimica Acta*, *65*(12), 1907–1919. https://doi.org/10.1016/s0016-7037(01)00570-1

Hugoni, M., Escalas, A., Bernard, C., Nicolas, S., Jezequel, D., Vazzoler, F., et al. (2018). Spatiotemporal variations in microbial diversity across the three domains of life in a tropical thalassohaline lake (Dziani Dzaha, Mayotte Island). *Molecular Ecology*, *27*(23), 4775–4786. https://doi.org/10.1111/mec.14901

Hulston, J. R., & McCabe, W. J. (1962). Mass spectrometer measurements in the thermal areas of New Zealand. Part 2. Carbon isotopic ratios. *Geochimica et Cosmochimica Acta*, *26*, 399–410. https://doi.org/10.1016/0016-7037(62)90110-2

Irwin, W. P., & Barnes, I. (1980). Tectonic relations of carbon dioxide discharges and earthquakes. *Journal of Geophysical Research*, *85*, 3115–3121. https://doi.org/10.1029/JB085iB06p03115

Jovovic, I., Grossi, V., Adam, P., Cartigny, P., Antheaume, I., Sala, D., et al. (2017). Early diagenesis and preservation of sedimentary organic matter in an anoxic, sulfidic lake (Lake Dziani Dzaha, Mayotte). In *28th International Meeting on organic geochemistry 17–22 September 2017, Florence, Italy*.

Klimke, J., Franke, D., Gaedicke, C., Schreckenberger, B., Schnabel, M., Stollhofen, H., et al. (2016). How to identify oceanic crust—Evidence for a complex break-up in the Mozambique Channel, off East Africa. *Tectonophysics*, *693*, 436–452. https://doi.org/10.1016/j.tecto.2015.10.012

Leboulanger, C., Agogue, H., Bernard, C., Bouvy, M., Carre, C., Cellamare, M., et al. (2017). Microbial diversity and cyanobacterial production in Dziani Dzaha crater lake, a unique tropical thalassohaline environment. *PloS One*, *12*(1), e0168879. https://doi.org/10.1371/journal.pone.0168879

Lemoine, A., Briole, P., Bertil, D., Roullé, A., Foumelis, M., Thinon, I., et al. (2020). The 2018–2019 seismo-volcanic crisis east of Mayotte, Comoros islands: Seismicity and ground deformation markers of an exceptional submarine eruption. *Geophysical Journal International*, *223*(1), 22–44. https://doi.org/10.1093/gji/ggaa273

Lénat, J.-F., Robineau, B., Durand, S., & Bachèlery, P. (1998). Etude de la zone sommitale du volcan Karthala (Grande Comore) par polarisation spontanée. *Compte-rendu de l'Académie des Sciences de Paris, Sciences de la Terre et des Planètes*, *327*, 781–788. https://doi.org/10.1016/s1251-8050(99)80051-2

Liuzzo, M., Di Muro, A., Giudice, G., Michon, L., Ferrazzini, V., & Gurrieri, S. (2015). New evidence of CO_2 soil degassing anomalies on Piton de la Fournaise volcano and the link with volcano tectonic structures. *Geochemistry, Geophysics, Geosystems*, *16*, 4388–4404. https://doi.org/10.1002/2015GC006032

Liuzzo, M., Gurrieri, S., Giudice, G., & Giuffrida, G. (2013). Ten years of soil CO_2 continuous monitoring on Mt. Etna: Exploring the relationship between processes of soil degassing and volcanic activity. *Geochemistry, Geophysics, Geosystems*, *14*, 2886–2899. https://doi.org/10.1002/ggge.20196

Marty, B. (2012). The origins and concentrations of water, carbon, nitrogen and noble gases on earth. *Earth and Planetary Science Letters*, *313*(314), 56–66. https://doi.org/10.1016/j.epsl.2011.10.040

Marty, B., Meynier, V., Nicolini, E., Griesshaber, E., & Toutain, J. P. (1993). Geochemistry of gas emanations: A case study of the Réunion Hot Spot, Indian Ocean. *Applied Geochemistry*, *8*, 141–152. https://doi.org/10.1016/0883-2927(93)90030-k

Marty, B., Pik, R., & Gezahegn, Y. (1996). Helium isotopic variations in Ethiopian plume lavas: Nature of magmatic sources and limit on lower mantle contribution. *Earth and Planetary Science Letters*, *144*(1–2), 223–237. https://doi.org/10.1016/0012-821x(96)00158-6

Mazzini, A., Svensen, H., Etiope, E., Onderdonk, N., & Banks, D. (2011). Fluid origin, gas fluxes and plumbing system in the sediment-hosted Salton Sea Geothermal System (California, USA). *Journal of Volcanology and Geothermal Research*, *205*, 67–83. https://doi.org/10.1016/j.jvolgeores.2011.05.008

Michon, L. (2016). The volcanism of the Comoros archipelago integrated at a regional scale. In P. Bachèlery, J.-F. Lénat, A. Di Muro, & L. Michon (Eds.), *Active volcanoes of the Southwest Indian Ocean: Piton de La Fournaise and Karthala* (pp. 333–344). Springer-Verlag, Berlin and Heidelberg. https://doi.org/10.1007/978-3-642-31395-0_21

Milesi, V. P., Debure, M., Marty, N. C. M., Capano, M., Jézéquel, D., Steefel, C., et al. (2020). Early diagenesis of lacustrine carbonates in volcanic settings: The role of magmatic CO_2 (Lake Dziani Dzaha, Mayotte, Indian Ocean). *ACS Earth and Space Chemistry*, *4*(3), 363–378. https://doi.org/10.1021/acsearthspacechem.9b00279

Milesi, V. P., Jézéquel, D., Debure, M., Cadeau, P., Guyot, F., Sarazin, G., et al. (2019). Formation of magnesium-smectite during lacustrine carbonates early diagenesis: Study case of the volcanic crater lake Dziani Dzaha (Mayotte–Indian Ocean). *Sedimentology*, *66*, 983–1001. https://doi.org/10.1111/sed.12531

Nehlig, P., Lacquement, F., Bernard, J., Audru, J., Caroff, M., Deparis, J., et al. (2013). *Notice explicative de la carte géologique Mayotte à 1/30.000 feuille Mayotte (1179)* (p. 74). BRGM.

Nougier, J., Cantagrel, J. M., & Karche, J. P. (1986). The Comoros archipelago in the western Indian Ocean: Volcanology, geochronology and geodynamic setting. *Journal of African Earth Sciences*, *5*(2), 135–145. https://doi.org/10.1016/0899-5362(86)90003-5

Ono, A., Sano, Y., Wakita, H., & Giggenbach, W. F. (1993). Carbon isotopes of methane and carbon dioxide in hydrothermal gases of Japan. *Geochemical Journal*, *27*(4–5), 287–295. https://doi.org/10.2343/geochemj.27.287

Ozima, M., & Podosek, F. A. (1983). *Noble gas geochemistry*. Cambridge University Press.

Paonita, A., Caracausi, A., Iacono-Marziano, G., Martelli, M., & Rizzo, A. (2012). Geochemical evidence for mixing between fluids exsolved at different depths in the magmatic system of Mt Etna (Italy). *Geochimica et Cosmochimica Acta*, *84*, 380–394. https://doi.org/10.1016/j.gca.2012.01.028

Paonita, A., Caracausi, A., Martelli, M., & Rizzo, A. L. (2016). Temporal variations of helium isotopes in volcanic gases quantify pre-eruptive refill and pressurization in magma reservoirs: The Mount Etna case. *Geology*, *44*(7), 499–502. https://doi.org/10.1130/g37807.1

Pelleter, A., Caroff, M., Cordier, C., Bachèlery, P., Nehlig, P., Debeuf, D., & Arnaud, N. (2014). Melilite-bearing lavas in Mayotte (France): An insight into the mantle source below the Comoros. *Lithos*, *208–209*, 281–297. https://doi.org/10.1016/j.lithos.2014.09.012

Phethean, J. J. J., Kalnins, L. M., van Hunen, J., Biffi, P. G., Davies, R. J., & McCaffrey, K. J. W. (2016). Madagascar's escape from Africa: A high-resolution plate reconstruction for the Western Somali Basin and implications for supercontinent dispersal. *Geochemistry, Geophysics, Geosystems*, *17*, 5036–5055. https://doi.org/10.1002/2016GC006624

Rabinowitz, P. D., Coffin, M. F., & Falvey, D. (1983). The separation of Madagascar and Africa. *Science*, *220*, 67–69. https://doi.org/10.1126/science.220.4592.67

Reid, R. C., Prausnitz, J. M., & Sherwood, T. K. (1977). *The properties of gases and liquids* (3rd ed.). McGraw-Hill.

REVOSIMA. (2019). *Bulletin n°1 de l'activité sismo-volcanique à Mayotte*. IPGP, Université de Paris, OVPF, BRGM, Ifremer, CNRS. Retrieved from http://www.ipgp.fr/sites/default/files/ipgp_1er_bulletin_info_sismo_volcanique_mayotte-cor.pdf

Rizzo, A. L., Caracausi, A., Chavagnac, V., Nomikou, P., Polymenakou, P. N., Mandalakis, M., et al. (2016). Kolumbo submarine volcano (Greece): An active window into the Aegean subduction system. *Scientific Reports*, *6*, 28013. https://doi.org/10.1038/srep28013

Rizzo, A. L., Caracausi, A., Chavagnac, V., Nomikou, P., Polymenakou, P. N., Mandalakis, M., et al. (2019). Geochemistry of CO_2-rich gases venting from submarine volcanism: The case of Kolumbo (Hellenic Volcanic Arc, Greece). *Frontiers of Earth Science*, *7*, 60. https://doi.org/10.3389/feart.2019.00060

Rizzo, A. L., Federico, C., Inguaggiato, S., Sollami, A., Tantillo, M., Vita, F., et al. (2015). The 2014 effusive eruption at Stromboli volcano (Italy): Inferences from soil CO_2 flux and $^3He/^4He$ ratio in thermal waters. *Geophysical Research Letters*, *42*, 2235–2243. https://doi.org/10.1002/2014GL062955

Roach, P., Milsom, J., Toland, C., Matchette-Downes, C., Budden, C., Riaroh, D., & Houmadi, N. (2017). *New evidence supports presence of continental crust beneath the Comoros: PESGB/HGS Africa Conference*.

Rouff, A. A., Phillips, B. L., Cochiara, S. G., & Nagy, K. L. (2012). The effect of dissolved humic acids on aluminosilicate formation and associated carbon sequestration. *Applied and Environmental Soil Science*, *2012*, 12. https://doi.org/10.1155/2012/430354

Sanjuan, B., Baltassat, J., Bezelgues, S., Brach, M., Girard, J., & Mathieu, F. (2008). *Estimation du potentiel géothermique de Mayotte: Phase 2-Étape 2. Investigations géologiques, géochimiques et géophysiques complémentaires, synthèse des résultats* (p. 82, 18 fig., 3 tabl., 6 ann). Rapport BRGM/RP-56802-FR.

Sano, Y., Kagoshima, T., Takahata, N., Nishio, Y., Roulleau, E., Pinti, D. L., & Fischer, T. P. (2015). Ten-year helium anomaly prior to the 2014 Mt Ontake eruption. *Scientific Reports*, *5*, 13069. https://doi.org/10.1038/srep13069

Sano, Y., & Marty, B. (1995). Origin of carbon in fumarolic gases from island arcs. *Chemical Geology*, *119*, 265–274. https://doi.org/10.1016/0009-2541(94)00097-R

Sano, Y., & Wakita, H. (1985). Geographical distribution of $^3He/^4He$ ratios in Japan: Implications for arc tectonics and incipient magmatism. *Journal of Geophysical Research*, *90*, 8729–8741. https://doi.org/10.1029/jb090ib10p08729

Schoell, M. (1980). The hydrogen and carbon isotopic composition of methane from natural gases of various origins. *Geochimica et Cosmochimica Acta*, *44*, 649–661. https://doi.org/10.1016/0016-7037(80)90155-6

Severinghaus, J. P., Bender, M. L., Keeling, R. F., & Broecker, W. S. (1996). Fractionation of soil gases by diffusion of water vapor, gravitational settling and thermal diffusion. *Geochimica et Cosmochimica Acta*, *60*, 1005–1018. https://doi.org/10.1016/0016-7037(96)00011-7

Spāth, A., Roex, A. P. L., & Duncan, R. A. (1996). The Geochemistry of Lavas from the Gomores Archipelago, Western Indian Ocean: Petrogenesis and mantle source region characteristics. *Journal of Petrology*, *37*(4), 961–991.

Taran, Y. A., Kliger, G. A., Cienfuegos, E., & Shuykin, A. N. (2010). Carbon and hydrogen isotopic compositions of products of open-system catalytic hydrogenation of CO_2: Implications for abiogenic hydrocarbons in Earth's crust. *Geochimica et Cosmochimica Acta*, *74*, 6112–6125. https://doi.org/10.1016/j.gca.2010.08.012

Traineau, H., Sanjuan, B., Brach, M., & Audru, J.-C. (2006). *Etat des connaissances du potentiel géothermique de Mayotte* (Rapport final). BRGM/RP-54700-FR.

Tzevahirtzian, A., Zaragosi, S., Bachèlery, P., Biscara, L., & Marchès, E. (2021). Submarine morphology of the Comoros volcanic archipelago. *Marine Geology*, *432*, 106383. https://doi.org/10.1016/j.margeo.2020.106383

Welhan, J. A. (1988). Origins of methane in hydrothermal systems. *Chemical Geology*, *71*, 183–198. https://doi.org/10.1016/0009-2541(88)90114-3

Zinke, J., Reijmer, J. J. G., & Thomassin, B. A. (2001). Seismic architecture and sediment distribution within the Holocene barrier reef–lagoon complex of Mayotte (Comoro archipelago, SW Indian Ocean). *Palaeogeography, Palaeoclimatology, Palaeoecology*, *175*(1–4), 343–368. https://doi.org/10.1016/s0031-0182(01)00379-0

Reference From the Supporting Information

Richet, P., Bottinga, Y., & Javoy, M. (1977). A review of hydrogen, carbon, nitrogen, oxygen, sulfur, and chlorine stable isotope fractionation among gaseous molecules. *Annual Review of Earth and Planetary Sciences*, *5*, 65–110. https://doi.org/10.1146/annurev.ea.05.050177.000433